

---

# From Coarse to Fine: A Physics-Informed Self-Guided Flow Diffusion Model

---

Ruoyan Li<sup>\*1</sup> Zijie Huang<sup>\*1</sup> Yizhou Sun<sup>1</sup> Wei Wang<sup>1</sup>

## Abstract

Machine learning methods, such as diffusion models, are widely explored as a promising way to accelerate high-fidelity fluid dynamics computation via a super-resolution process from faster-to-compute low-fidelity input. However, existing approaches usually made impractical assumption that the low-fidelity data is down-sampled from high-fidelity data. In reality, low-fidelity data is produced by numerical solvers that use a coarser resolution. Solver-generated low-fidelity data usually sacrifices fine-grained details, such as small-scale vortices compared to high-fidelity ones. Our findings show that SOTA diffusion models struggle to reconstruct fine-scale details when faced with solver-generated low-fidelity inputs. To bridge this gap, we propose PG-Diff, a novel diffusion model for reconstruction, where both low- and high-fidelity data are generated from numerical solvers. We propose an *Importance Weight* strategy during training that serves as a form of self-guidance, and a training-free *Residual Correction* approach during inference that embeds physical insights into the model. Together, these techniques steer the diffusion model toward more accurate reconstructions. Experimental results on four 2D turbulent flow datasets demonstrate the efficacy of our proposed method. Code is available [here](#).

## 1. Introduction

High-fidelity simulations of computational fluid dynamics (CFD) are crucial for understanding fluid interactions in engineering systems, greatly impacting design and application outcomes (Wang et al., 2024). Traditional approaches such as Direct Numerical Simulation (DNS) offer high-resolution solutions. However, they are computationally expensive, especially for turbulence with high Reynolds numbers (Zhang

et al., 2023). Therefore, learning neural-based simulators from data becomes attractive alternative, balancing between efficiency and simulation fidelity (Huang et al., 2023).

One popular strategy is to reconstruct high-fidelity data from low-fidelity inputs, where the input data usually reduces the discretization grid size in the spatial domain thus is computational-efficient (Shu et al., 2023; Pradhan & Duraisamy, 2021). Various machine learning models, including those based on Convolutional Neural Networks (CNNs) (Fukami et al., 2019), Generative Adversarial Networks (GANs) (Li & McComb, 2022), and Diffusion Models (Shu et al., 2023), have been developed to reconstruct high-fidelity CFD data from low-fidelity inputs. Majority of them are categorized as direct mapping models, which require both low- and high-fidelity data for training and can only capture a particular resolution mapping. In contrast, diffusion models only require high-fidelity data during training and use low-fidelity data as intermediate samples in the denoising stage as guidance for reconstruction (Shu et al., 2023). Therefore, they can reconstruct from low-fidelity data at any resolution without retraining.

One fundamental drawback in existing works is that they assume low-fidelity data is artificially downsampled from high-fidelity data at the same timestamp. Such data inherently has more information compared to solver-generated low-fidelity data in reality, where coarser discretization grids are used in numerical solvers to save computational resources. As illustrated in Figure 1, the former follows “integrate then downsample”, which starts from the high-fidelity initial states to rollout trajectories, and then downsample at each timestamp. The latter follows “downsample then integrate”, which downsamples the high-fidelity initial state to obtain coarser discretization grids as starting points and rollout trajectories through numerical solvers. Therefore, models evaluated in downsampled settings can lead to unreliable conclusions, as solver-generated low-fidelity data retain less information from high-fidelity data. This is illustrated by the visualization of low-fidelity data generated from the two: the downsampled one contains more fine-grained details than the solver-based one.

We study how to use diffusion model for reconstructing high-fidelity CFD data from solver-generated low-fidelity data with coarser discretization grids. Our experiments reveal

<sup>\*</sup>Equal contribution <sup>1</sup>University of California, Los Angeles, Department of Computer Science. Correspondence to: Wei Wang <weiwang@cs.ucla.edu>.

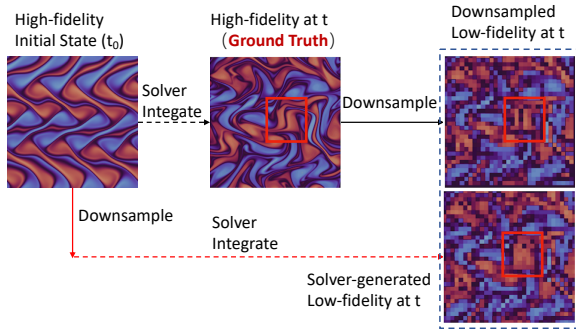


Figure 1. Comparison between downsampled (black line) and solver-generated (red line) flow fields. Solver-generated low-fidelity data retain less information, especially for fine-grained high-fidelity details.

that SOTA diffusion models struggle to recover fine-grained high-fidelity details given solver-generated low-fidelity inputs, and we also analytically show why they fail. In response to this challenge, we build upon this state-of-the-art model by Shu et al. (2023) and propose an *Importance Weight* strategy during training as self-guidance to locate fine-grained high-fidelity details, and a training-free *Residual Correction* module during inference for injecting physical inductive bias. The two modules jointly guide the diffusion model toward higher-quality reconstructions. Specifically, the *Importance Weight* module assigns importance scores to different components in the flow field through Discrete Wavelet Transformation (DWT) (Daubechies, 1992a), which are integrated into the loss function for guiding the diffusion model to better reconstruct detailed and accurate structures. The *Residual Correction* module projects the reconstructed samples onto the solution subspace of the governing equations, ensuring that the generated outputs also adhere to physical constraints such as Navier-Stokes Equations (Navier, 1823). We achieve this by applying gradient descent of the residuals of the governing equations at certain diffusion steps, to refine the generated high-fidelity data. We also explore different scheduling strategies on which diffusion steps to apply such correction. Our findings suggest that applying residual corrections at both the beginning and the end of diffusion steps strikes the ideal balance between reconstruction error and physical coherence.

Our key contributions are summarized as follows:

- We study a novel problem on reconstructing high-fidelity flow fields with solver-generated low-fidelity data. Our evidence reveals that SOTA diffusion models fail to generate high-quality outputs due to the loss of fine-grained detail in low-fidelity data.
- In light of this issue, we propose PG-Diff, which builds upon the SOTA diffusion model with the guidance of an *Importance Weight* strategy during training as

self-guidance and a training-free *Residual Correction* method during inference as physical inductive bias.

- We present empirical evidence of PG-Diff’s superior performance in a variety of 2D turbulent flow over 4 datasets. It yields a significant improvement in terms of predictive accuracy physical consistency, and perceptual quality.

## 2. Preliminaries and Related Work

We consider a machine learning model  $f_\theta : \mathcal{X} \rightarrow \mathcal{Y}$  with parameters  $\theta$ , which transforms a data sample from low-fidelity domain  $x \in \mathcal{X} \subseteq \mathbb{R}^{m \times m}$  to high-fidelity domain  $y \in \mathcal{Y} \subseteq \mathbb{R}^{n \times n}$  ( $m < n$ ). The distributions of the training and test sets for low-fidelity data are denoted by  $p_{\mathcal{X}}^{\text{train}}$  and  $p_{\mathcal{X}}^{\text{test}}$ , respectively, and for high-fidelity data as  $p_{\mathcal{Y}}^{\text{train}}$  and  $p_{\mathcal{Y}}^{\text{test}}$ . The training and testing distribution for low and high-fidelity data are not necessarily identical. The objective is to develop  $f_\theta$  such that it can effectively map samples from  $\mathcal{X}^{\text{test}}$  to their corresponding high-fidelity counterparts  $\mathcal{Y}^{\text{test}}$ . As diffusion model operates on the same input and output grid, we upsample the low-fidelity data uniformly during inference as the model input.

### 2.1. AI for Computational Fluid Dynamics (CFD)

Recent advances in machine learning have led to various learning-based surrogate models for accelerating scientific discoveries (Sanchez-Gonzalez et al., 2020; Li et al., 2020; 2021). In the field of high-fidelity CFD reconstruction, researchers have developed powerful models rooted in image super-resolution domain in computer vision. Specifically, GANs (Ledig et al., 2016; Wang et al., 2019) and normalizing flows (Lugmayr et al., 2020) have achieved impressive results for image reconstruction. Later on, diffusion models (Saharia et al., 2021) have challenged the long-standing dominance of GANs. Various physical inductive biases (Raissi et al., 2019; Bai et al., 2020; Chen et al., 2021) have been injected into these methods for CFD reconstructions, which enhances the robustness and accuracy of the reconstruction task. For example, Ren et al. (2023); Jiang et al. (2020) leveraged CNN for spatial-temporal super resolution. Fukami et al. (2021) adapted existing CNN models for use with moving sensors. Li & McComb (2022) further advanced the field by proposing physics-informed GANs. Additionally, Fu et al. (2023) proposed a refinement network to address the issue with limited high-fidelity data. These models rely on low- and high-fidelity data pairs during training and can only capture specific resolution mappings. As a result, when the test data deviates significantly from the

<sup>1</sup>For direct mapping models, the training takes low- and high-fidelity pairs as inputs. For diffusion models, the training only requires high-fidelity data, and low-fidelity data is used as input during testing.

training data, their performance degrades. To overcome this limitation, Gao et al. (2021) utilizes physical properties of the fluid such as conservation laws and boundary conditions for super resolution. Shu et al. (2023) leveraged diffusion model, which is trained exclusively on high-fidelity data and enables reconstruction from any type of low-fidelity input. However, these methods assume the low-fidelity data is artificially downsampled from high-fidelity sources, which limits their performance during inference when reconstructing from solver-generated low-fidelity data in reality. While the evaluation of CFD super-resolution models on solver-generated low-fidelity data was conducted by Sarkar et al. (2023), the U-net model examined in their study corresponds to direct mapping approaches, which utilize both low- and high-fidelity data during training to learn a specific resolution mapping. In contrast, the state-of-the-art diffusion model proposed by Shu et al. (2023) does not incorporate low-fidelity data during training, instead modeling only the distribution of high-fidelity data. Consequently, the use of solver-generated low-fidelity data, as proposed by Sarkar et al. (2023), is not applicable to diffusion models.

## 2.2. Denoising Diffusion Probabilistic Model

Diffusion models have become a prominent class of deep generative models, demonstrating state-of-the-art performance across various domains such as image generation (Meng et al., 2022; Saharia et al., 2021; Ho et al., 2020), video synthesis (Yang & Hong, 2022; Yu et al., 2022), 3D shape creation (Zhou et al., 2021; Zeng et al., 2022), and applications in scientific fields (Shu et al., 2023; Yang & Sommer, 2023; Qiu et al., 2024). Denoising Diffusion Probabilistic Models (DDPMs) are grounded in a stochastic diffusion process, akin to those found in thermodynamics. It contains a forward and reverse process, where a data sample is gradually corrupted with noise via a Markov chain, and a neural network is trained to reverse this, progressively removing the noise. To generate new samples, a fully noisy input is denoised by the model step by step.

Formally, in the forward diffusion process, the input data  $x_0$  is gradually corrupted with Gaussian noises as  $q(x_t|x_{t-1}) = \mathcal{N}(x_t; \sqrt{1 - \beta_t}x_{t-1}, \beta_t\mathbf{I})$  ( $t = 1, 2, \dots, T$ ), where  $\beta_1, \dots, \beta_T$  are fixed variance schedule that control the amount of noise introduced at each step,  $T$  is the number of total diffusion steps and  $q(x_t|x_{t-1})$  is the Markov transition probability. Let  $\bar{\alpha}_t := \prod_{s=1}^t 1 - \beta_s$ , we have  $x_t = \sqrt{\bar{\alpha}_t}x_0 + \sqrt{1 - \bar{\alpha}_t}\epsilon_t$ , which describes how to generate noisy states  $x_t$  from input  $x_0$ . The reverse process is defined as  $p_\theta(x_{t-1}|x_t) = \mathcal{N}(x_{t-1}; \mu_\theta(x_t, t), \Sigma_\theta(x_t, t))$ , where  $\mu_\theta$  and  $\Sigma_\theta$  are learned by neural networks parameterized by  $\theta$ , and  $p_\theta(x_{t-1}|x_t)$  is the denoising transition probability, undoing the transformation in the forward process.

Training DDPM involves minimizing a variational bound

on the negative log-likelihood of  $q(x_0)$ . Ho et al. (2020) showed that it can be simplified as predicting the noise at each step:

$$L^{\text{simple}} = \mathbb{E}_{t, x_0, \epsilon} [\|\epsilon_t - \epsilon_\theta(\sqrt{\bar{\alpha}_t}x_0 + \sqrt{1 - \bar{\alpha}_t}\epsilon_t, t)\|^2], \quad (1)$$

where  $\epsilon_\theta(\cdot)$  is the predicted noise from DDPM’s denoiser neural network. The denoiser takes noised sample  $x_t = \sqrt{\bar{\alpha}_t}x_0 + \sqrt{1 - \bar{\alpha}_t}\epsilon_t$  and diffusion timestamp  $t$  as input to predict noise at each timestamp.  $\epsilon_t \sim \mathcal{N}(\mathbf{0}, \mathbf{I})$  is the standard Gaussian noise sampled at time  $t$ . In this paper, we implement the backbone diffusion model proposed by Ho et al. (2020) and apply accelerated sampling techniques introduced by Song et al. (2020).

## 3. Method:PG-Diff

We build upon the diffusion framework proposed by Shu et al. (2023) and experiment on reconstructing high-fidelity CFD from solver-generated low-fidelity input, which has more information loss compared to artificially downsampled low-fidelity inputs. Our model, PG-Diff, features an *Importance Weight* strategy that scores different components in the flow fields through the loss function as self-guidance, forcing the model to recover more fine-grained high-fidelity details during training. In addition, a training-free *Residual Correction* module applies physics-informed correction during inference, ensuring physical coherence in reconstructed samples. The two modules jointly guide the model toward high-quality reconstruction from a wide-range of low-fidelity inputs. The overall framework is depicted in Figure 2. We now introduce each component in detail.

**Model Setup.** PG-Diff follows the guided data synthesis setting for CFD reconstruction as in Shu et al. (2023): we train the model via recovering high-fidelity sources only, and condition on low-fidelity inputs as intermediate diffusion step during inference. This brings two benefits: (1) exerting control over the reconstruction process during inference. Instead of starting from random noises, the reverse diffusion starts from low-fidelity inputs as intermediate diffusion steps. (2) The model can reconstruct from generalized low-fidelity data, since the training does not depend on low- and high-fidelity pairs as in direct mapping models.

Formally, during the training forward process, we obtain intermediate diffusion states  $x_t$  via the following, where  $x_t$  represents the noisy version of high-fidelity sample at forward diffusion step  $t$ . Here  $y \sim p_y^{\text{train}} := x_0$  is the high-fidelity CFD we want to recover.  $\epsilon_t \sim \mathcal{N}(\mathbf{0}, \mathbf{I})$  is the standard Gaussian noise sampled at time  $t$  and  $\bar{\alpha}_t := \prod_{s=1}^t 1 - \beta_s$  as introduced in Sec 2.2.

$$x_t = \sqrt{\bar{\alpha}_t}x_0 + \sqrt{1 - \bar{\alpha}_t}\epsilon_t = \sqrt{\bar{\alpha}_t}y + \sqrt{1 - \bar{\alpha}_t}\epsilon_t \quad (2)$$

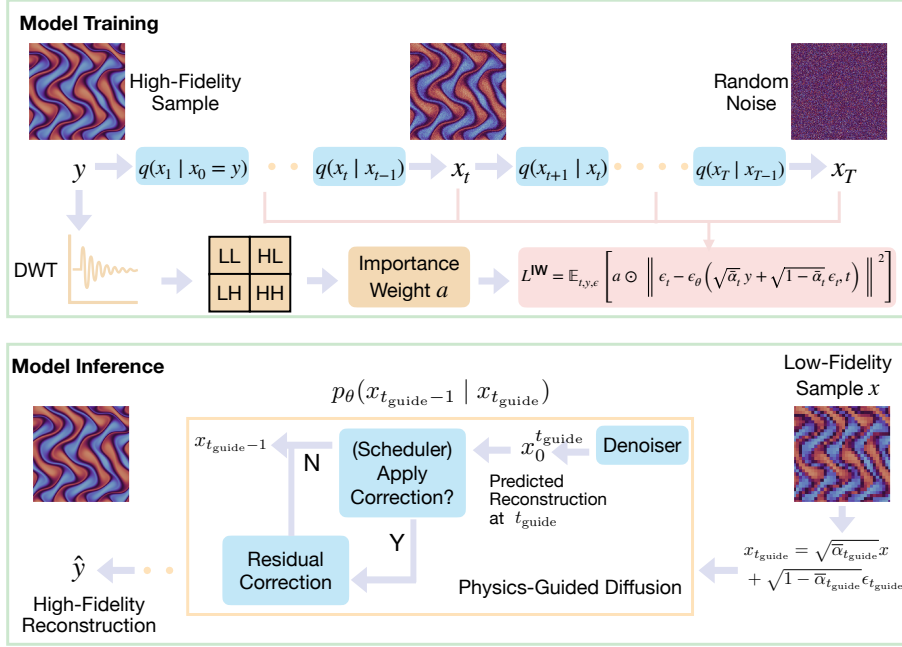


Figure 2. Training and inference pipeline of PG-Diff. Training with high-fidelity data only, guided by importance weight strategy to locate fine-grained high-fidelity details. During inference, low-fidelity data is used for reconstruction, and residual correction is applied at intermediate diffusion steps to improve physical coherence. We follow (Ho et al., 2020) and use U-net as our denoiser.

During the inference stage, we first obtain the intermediate diffusion state  $x_{t_{\text{guide}}}$  ( $0 < t_{\text{guide}} < T$ ) by adding noises to the conditioned low-fidelity data  $x \sim p_{\mathcal{X}}^{\text{est}}$  as

$$x_{t_{\text{guide}}} = \sqrt{\bar{\alpha}_{t_{\text{guide}}}} x + \sqrt{1 - \bar{\alpha}_{t_{\text{guide}}}} \epsilon_{t_{\text{guide}}}. \quad (3)$$

We adopt the same  $t_{\text{guide}}$  as Shu et al. (2023), and use  $x_{t_{\text{guide}}}$  as the starting point for the reverse process to reconstruct the high-fidelity sources. Equivalently, this means the reverse diffusion starts from  $t_{\text{guide}}$  instead of  $T$ . The reverse diffusion process progressively produces a refined high-fidelity reconstruction that aligns with the low-fidelity conditioning data, using the following DDIM (Song et al., 2020) sampling formula for acceleration.

$$x_{t-1} = \sqrt{\bar{\alpha}_{t-1}} x_0^t + \sqrt{1 - \bar{\alpha}_{t-1} - \sigma_t^2 \epsilon_\theta(x_t, t) + \sigma_t^2 \epsilon_t} \quad (4)$$

Here  $0 < t < t_{\text{guide}}$  and  $x_0^t = \frac{x_t - \sqrt{1 - \bar{\alpha}_t} \epsilon_\theta(x_t, t)}{\sqrt{\bar{\alpha}_t}}$  is the reconstructed high-fidelity data from  $x_t$  at each reverse diffusion step  $t$  via de-noising.

Shu et al. (2023) applied the above procedure to reconstruct high-fidelity data from artificially downsampled low-fidelity input. We demonstrate in Proposition 3.1 why their proposed diffusion model performs poorly when reconstructing solver-generated low-fidelity data. For solver-generated

low-fidelity data, the differences in probability distributions become larger, which hinders diffusion model’s ability for accurate reconstruction. We show the detailed proof in Appendix E.10.

**Proposition 3.1.** *Let  $p_{\mathcal{Y}}$  denote the probability distribution of high-fidelity data. Let  $p_{\mathcal{X}}$  and  $q_{\mathcal{X}}$  denote the probability distribution of solver generated and downsampled low-fidelity data respectively. Then, it follows that*

$$D_{KL}(p_{\mathcal{Y}} \| p_{\mathcal{X}}) \geq D_{KL}(p_{\mathcal{Y}} \| q_{\mathcal{X}})$$

### 3.1. Importance Weight During Training

Existing diffusion models can fail to capture fine-grained details when conditioned on solver-generated low-fidelity data. We therefore introduce an importance weighting mechanism during training as self-guidance to address this limitation. Specifically, we transform the high-fidelity data into the wavelet domain using the DWT and assign importance scores to different components of fluid fields within the diffusion loss function. By considering spatial relationships between nearby vorticity values, DWT has great abilities to locate information both in spatial and frequency domains (Daubechies, 1992b; Akansu & Haddad, 1992), thus allowing the model to capture fine-grained structures effectively. Formally, we decompose fluid fields  $y \in \mathcal{R}^{n \times n}$  into frequency subdomains and compute the sum of squares of the high-frequency modes – namely HL (high-low), LH (low-high) and HH (high-high) subdomains as below,

where  $HL, LH, HH, F \in \mathbb{R}^{\frac{n}{2} \times \frac{n}{2}}$ . HL captures horizontal high-frequency signals, while LH captures vertical high-frequency signals. HH captures high-frequency signals in both directions, corresponding to diagonal details such as intersections. Details about DWT are in Appendix C.1.

$$F = HL^2 + LH^2 + HH^2. \quad (5)$$

To compute importance scores, we then uniformly upsample  $F$  to  $\hat{F} \in \mathbb{R}^{n \times n}$  and linearly map  $\hat{F}_{i,j}$  to an importance weight  $a_{i,j}$  as below, where  $\alpha, \beta$  are the minimum and maximum importance weight value respectively,  $Q_\theta(\hat{F}) \in \mathbb{R}$  is the  $\theta$  quantile of all  $\hat{F}$  values.

$$a_{i,j} = \begin{cases} \alpha + (\beta - \alpha) \frac{\hat{F}_{i,j} - Q_\theta(\hat{F})}{\max \hat{F} - Q_\theta(\hat{F})} & \text{if } \hat{F}_{i,j} > Q_\theta(\hat{F}) \\ 1 & \text{otherwise} \end{cases} \quad (6)$$

If  $\hat{F}_{i,j}$  exceeds the  $\theta$  quantile of all  $\hat{F}$  values, the corresponding component is considered high-frequency, and will be assigned with weight greater than 1. Finally, the diffusion loss function in Eqn 1 is updated to incorporate the importance weighting as follows:

$$L^{IW} = \mathbb{E}_{t,y,\epsilon} \left[ a \odot \|\epsilon_t - \epsilon_\theta (\sqrt{\bar{\alpha}_t} y + \sqrt{1 - \bar{\alpha}_t} \epsilon_t, t)\|^2 \right], \quad (7)$$

where  $\epsilon_\theta$  represents the denoiser,  $\epsilon_t$  is the ground truth noise at time  $t$ , and  $\odot$  denotes element-wise multiplication.

**Importance Weight Design Choice.** Our *importance weight* strategy is incorporated exclusively during training, ensuring that the model focuses on regions with high-frequency details. The DWT-based calculation avoids the large computational complexity often associated with attention mechanisms. It efficiently emphasizes important features by leveraging the intrinsic properties of the wavelet transform, resulting in a more targeted learning process.

### 3.2. Residual Correction During Inference

In addition, we introduce a physics-informed residual correction module to enhance the physical coherence of the reconstructed data during inference. In the reverse diffusion process, we apply such correction to refine the reconstructed high-fidelity data at selected steps determined by a scheduling policy. Since we use DDIM (Song et al., 2020) for acceleration, we represent the sampled diffusion states as  $x^\tau$ , and its corresponding reconstruction as  $x_0^\tau$  ( $\tau < t_{\text{guide}}$ ) in the following. Note that we do not apply correction on the noisy state  $x^\tau$  ( $\tau < t_{\text{guide}}$ ) directly. The correction is to perform gradient descent based on the residuals  $\mathcal{R}$  of the governing PDEs as  $\mathcal{R} = \frac{1}{N} \sum_{i,j} [\text{LHS}_{i,j} - \text{RHS}_{i,j}]^2$ , where LHS and RHS represent the left- and right-hand side of the PDE, respectively.  $N$  represents the number of grid

points. The key parameters in this process are the residual correction schedule policy (the specific diffusion steps at which the correction is applied), the number of gradient descent steps  $N$ , and the step size  $\eta$ , which we study their impacts in Section 4.5. Our findings suggest that applying residual corrections at both the beginning and the end of diffusion steps strikes the ideal balance between reconstruction L2 error and the physical coherence. We utilize the Adam algorithm (Kingma & Ba, 2015) for the gradient descent and summarize the physics-guided inference procedure using DDIM (Song et al., 2020) in Algorithm 1.

One existing work proposes a conditional diffusion model (Shu et al., 2023), where residual at every training diffusion step is concatenated with the current state to generate the diffusion state at next timestamp, serving as the condition. One key advantage of PG-Diff is that it is training-free, allowing the correction process to be applied without additional learning to the original diffusion model. Also, our approach offers the flexibility to adjust the residual correction schedule dynamically. This adaptability enables an optimal balance between predictive accuracy and physical consistency of the reconstructed sample. We empirically show our method achieves better performance in Sec 4.3. Additionally, diffusion model guided generation has been widely studied in Chung et al. (2023); Huang et al. (2024); Zhu et al. (2023); Shysheya et al. (2024), our Residual Correction differs by applying guidance to **denoised samples** instead of noisy samples and involves multiple steps of gradient descent at **selected backward diffusion steps**, in contrast to a single step of gradient descent applied at every backward diffusion step in other works.

## 4. Experiments

### 4.1. Dataset

We generated four 2D turbulent flow datasets with different characteristics: 1.) *Taylor Green Vortex*, featuring how vortices diminish in turbulent flows, where large-scale vortices gradually break down into smaller turbulent structures; 2.) *Decaying Turbulence*, describing turbulence that evolves naturally without external forces. As time progresses, the turbulence weakens due to viscous effects; 3.) *Kolmogorov Flow*, which portrays turbulence influenced by a sinusoidal external force combined with a drag component; 4.) *McWilliams Flow* (McWilliams, 1984), which describes the behavior of isolated vortices in turbulent conditions. It is the most challenging one, demanding accurate modeling of inverse energy transfer and multi-scale vortex interactions.

The four datasets are generated by the incompressible

**Algorithm 1** Physics-informed Training-free Correction with DDIM during Inference.

**Require:**  $x \in \mathcal{X}^{\text{test}}$  (guide),  $t_{\text{guide}}$  ( $t_{\text{guide}} < T$ ),  $\tau = \{\tau_0, \tau_1, \dots, \tau_K\}$  (backward diffusion timestamp, where  $\tau_0 = 0, \dots, \tau_K = t_{\text{guide}}$ ),  $\epsilon_\theta$  (denoiser),  $\mathcal{R}(\cdot)$  (PDE residual),  $N$  (gradient descent steps),  $\eta$  (step size).

- 1:  $\epsilon_{\tau_K} \sim \mathcal{N}(0, I)$  #  $\tau_K = t_{\text{guide}}$
- 2:  $x_{\tau_K} = \sqrt{\bar{\alpha}_{\tau_K}}x + \sqrt{1 - \bar{\alpha}_{\tau_K}}\epsilon_{\tau_K}$  # Adding noises to low-fidelity input via forward diffusion
- 3: **for**  $i = K, K-1, \dots, 1, 0$  **do**
- 4:  $x_0^{\tau_i} = \frac{x_{\tau_i} - \sqrt{1 - \bar{\alpha}_{\tau_i}}\epsilon_\theta(x_{\tau_i}, \tau_i)}{\sqrt{\bar{\alpha}_{\tau_i}}}$  # Predicted reconstruction ( $x_0$ ) at  $\tau_i$
- 5: **if** correction is performed at time  $\tau_{i-1}$  **then**
- 6:     **repeat**
- 7:          $x_0^{\tau_i} = x_0^{\tau_i} - \eta \cdot \text{Adam}(\nabla \mathcal{R}(x_0^{\tau_i}))$  # Residual-Based Correction
- 8:     **until**  $N$  times
- 9:     **end if**
- 10:  $x_{\tau_{i-1}} = \sqrt{\bar{\alpha}_{\tau_{i-1}}}x_0^{\tau_i} + \sqrt{1 - \bar{\alpha}_{\tau_{i-1}} - \sigma_{\tau_i}^2}\epsilon_\theta(x_{\tau_i}, \tau_i) + \sigma_{\tau_i}^2\epsilon_{\tau_i}$  #  $x_{\tau_{i-1}} \sim p_\theta(x_{\tau_{i-1}}|x_{\tau_i})$
- 11: **end for**

Navier-Stokes equations following (Li et al., 2021)

$$\frac{\partial \omega(\mathbf{x}, t)}{\partial t} + \mathbf{u}(\mathbf{x}, t) \cdot \nabla \omega(\mathbf{x}, t) = \frac{1}{Re} \nabla^2 \omega(\mathbf{x}, t) + f(\mathbf{x}),$$

$$\nabla \cdot \mathbf{u}(\mathbf{x}, t) = 0, \quad \omega(\mathbf{x}, 0) = \omega_0(\mathbf{x}),$$

represents the vorticity,  $\mathbf{u}$  denotes the velocity field,  $Re$  is the Reynolds number, and  $f(\mathbf{x})$  is an external forcing term.  $\omega_0$  represents the initial vorticity distribution. The PDE is numerically solved by pseudo-spectral solver (Orszag, 1972) on equispaced discretization grids. The high-fidelity data are generated with  $2048 \times 2048$  discretization grid and then uniformly downsampled to  $256 \times 256$ , while those on the lower-resolution grids are considered low-fidelity. For each dataset, we use 80% of the trajectories for training, 10% for validation, and 10% for testing. More details can be found in Appendix D. Note that PG-Diff also utilizes the PDE for residual correction discussed in Sec 3.2.

## 4.2. Experiment Settings

**Task Setup and Baselines.** We evaluate two reconstruction settings with different low-fidelity resolutions:  $64 \times 64 \rightarrow 256 \times 256$  ( $4\times$  upsampling) and  $32 \times 32 \rightarrow 256 \times 256$  ( $8\times$  upsampling). To benchmark our approach, we compared against both direct mapping models and diffusion models: bicubic interpolation (Gonzalez & Woods, 2007), a CNN-based model (Fukami et al., 2019), a GAN-based model (Li & McComb, 2022), the vanilla diffusion model (Diff) and its conditional variant (Cond Diff) from Shu et al. (2023). In addition, we perform two ablation studies, namely PG-Diffw/o IW and PG-Diffw/o Cor, where we remove *Importance Weight* and *Residual Correction* respectively. More implementation details are provided in Appendix C.2.

**Evaluation Metrics.** We assess the reconstructed flow fields using three key metrics. We first use two standard metrics suggested by Shu et al. (2023): L2 norm for measuring the pointwise error between prediction and ground truth;

unnormalized residuals of the governing equation (Res.) for assessing adherence to the underlying physics. In addition, we conduct a novel multi-scale evaluation using DWT: we transform the predicted and ground truth flow fields into wavelet space and decompose them into four subdomains: LL (low-low), LH (low-high), HL (high-low), and HH (high-high). The LL subdomain captures large-scale, low-frequency information, while LH, HL, and HH encompass higher-frequency details like turbulent structures. By calculating the L2 norm in each subdomain, we gain a comprehensive understanding of the model’s performance across different scales, ensuring accurate reconstruction of both global flow features and fine-scale details.

## 4.3. Reconstruction Results

Table 1 reports the mean and standard deviation of L2 and PDE residual across datasets and models. For both up-sampling scales ( $32 \times 32 \rightarrow 256 \times 256$  and  $64 \times 64 \rightarrow 256 \times 256$ ), PG-Diff consistently outperforms baselines, showing its effectiveness. Notably, it achieves 3.5% to 7.7% performance gain against baselines in the  $4\times$  upsampling setting. The lower L2 achieved by PG-Diff indicates that it effectively captures essential features and dynamics of the turbulent flows. We present the residual of high-fidelity data in Table 4 in Appendix D, which demonstrates that residuals from PG-Diff reconstructions are closer to those of the high-fidelity data. The small difference in PDE residuals indicates that PG-Diff’s predictions adhere more closely to the underlying physical laws. Reconstructions from direct mapping models (GAN, CNN) exhibit significant deviations in physical coherence. For complex datasets dominated by fine-grained details, such as *Kolmogorov Flow* and *McWilliams Flow*, PG-Diff outperforms baselines by a margin, showing better reconstruction accuracy and physical coherence. Through ablation studies, we demonstrate that both *Importance Weight* and *Residual Correction* contribute

		Bicubic*	CNN	GAN	Diff	Cond Diff	PG-Diff	PG-Diff w/o Cor	PG-Diffw/o IW
<i>Taylor Green Vortex</i>	L2	6.08	<b>3.10±0.07</b>	3.36±0.08	3.28±0.01	4.50±0.04	3.18±0.01	3.20±1e-4	3.22±0.01
	Res.	2.18e4	1.40e5±3.6e4	4.54e4±1.3e4	4.17e4±3.3e3	<u>1.36e3±42</u>	<b>5.31e3±40</b>	7.44e4±1.4e4	6.95e3±569
<i>Taylor Green Vortex</i>	L2	3.04	2.99±0.06	2.83±0.3	1.68±2e-3	3.57±0.02	<b>1.55±9e-3</b>	1.57±0.02	1.59±6e-3
	Res.	1.05e4	1.37e5±3.6e4	4.18e4±1.1e4	<u>3.06e4±4.3e3</u>	1.47e5±1.9e4	<b>4.39e3±3</b>	6.67e4±8.4e3	6.09e3±9
<i>Decaying Turbulence</i>	L2	3.62	1.81±0.1	2.09±0.02	1.84±1e-3	2.02±8e-4	<b>1.78±1e-3</b>	1.78±2e-3	1.79±3e-3
	Res.	3.41e3	3.05e3±500	<u>7.63e2±111</u>	9.97e3±460	3.49e4±1.7e4	<b>1.65e2±11</b>	9.86e2±165	2.84e2±22
<i>Decaying Turbulence</i>	L2	1.74	1.66±0.1	2.06±0.05	0.85±6e-4	1.34±7e-4	<b>0.82±1e-3</b>	0.83±6e-3	0.83±4e-3
	Res.	1.31e3	3.16e3±781	<u>6.65e2±59</u>	4.33e3±164	1.52e4±161	<b>85±0.9</b>	2.76e3±1.5e3	1.87e2±37
<i>Kolmogorov Flow</i>	L2	4.71	3.02±8e-3	3.14±0.04	<u>3.09±1e-3</u>	3.13±1e-3	<b>2.78±8e-3</b>	2.82±1e-3	2.93±5e-4
	Res.	2.63e3	3.52e3±125	3.30e2±87	1.80e2±22	<u>80±2</u>	<b>40.12±0.3</b>	6.68e2±10	1.40e2±83
<i>Kolmogorov Flow</i>	L2	3.22	2.22±0.01	3.02±0.04	1.79±1e-3	<u>1.79±1e-3</u>	<b>1.66±4e-3</b>	1.69±8e-4	1.73±1e-3
	Res.	1.86e4	7.30e2±49	3.03e2±92	3.09e2±29	<u>1.65e2±7</u>	<b>39±0.06</b>	9.27e2±1	3.33e2±145
<i>McWilliams Flow</i>	L2	3.19	<b>2.00±0.07</b>	2.03±0.05	2.23±4e-3	2.24±5e-4	<u>2.04±2e-4</u>	2.06±3e-5	2.16±3e-4
	Res.	3.35e2	6.50e2±180	2.86e2±51	16±0.9	<u>12±1</u>	<b>5.5±4e-3</b>	66±1	7.8±0.2
<i>McWilliams Flow</i>	L2	2.17	1.75±0.1	1.96±0.08	<u>1.29±3e-4</u>	1.30±4e-4	<b>1.24±9e-5</b>	1.27±1e-4	1.30±2e-4
	Res.	2.17e2	3.64e2±127	2.42e2±35	<u>21±4</u>	31±4	<b>6.36±2e-3</b>	88±0.7	12±0.06

Table 1. Quantitative performance comparison over four datasets on L2 and Res. Results are repeated three times. Metrics are reported for both  $32\times 32 \rightarrow 256\times 256$  (gray) and  $64\times 64 \rightarrow 256\times 256$  tasks. **Bold** values indicate the best performance and underlined values represent the second-best. \* Bicubic interpolation is a deterministic algorithm, which has zero standard deviation.

significantly in improving model’s performance, underscoring the effectiveness of our design choices in capturing the complex behaviors of turbulent flows.

**Multi-Scale Evaluation.** In addition, we assess the model’s ability to capture flow structures at different scales using DWT. As shown in Figure 10 in Appendix E.2, PG-Diff demonstrates superior performance in the LL, LH, and HL subdomains, achieving the best or near-best results among all methods. Excelling in the LL subdomain indicates a strong capability in capturing large-scale, low-frequency components of the turbulent flows. The superior performance in the LH and HL subdomains suggests the effectiveness of PG-Diff in capturing small-scale vortices and transitions between scales. While direct mapping models exhibit better performance in the HH subdomain, PG-Diff’s results are close to those best-performing methods. The balanced performance across all subdomains demonstrates that PG-Diff can reconstruct both large-scale structures and fine-grained details essential for turbulent flows. Additional details on other datasets are presented in the Appendix E.2.

**Runtime Comparison.** We report the runtime comparison of different methods in Appendix E.8. PG-Diff only increases small inference time while achieving superior performance improvement against baselines. The total runtime of using the numerical solvers to generate low-fidelity data, and then reconstructing with PG-Diff is considerably faster than the time required to produce samples with similar error, demonstrating the effectiveness of PG-Diff.

**Sensitivity Analysis.** We study the effects of three key hyperparameters in calculating the importance weight in Sec 3.1: the maximum importance weight  $\beta$ , minimum

importance weight  $\alpha$ , and the threshold parameter  $\theta$ . The results in Appendix E.5 show that increasing  $\beta$  reduces both L2 and PDE residuals, indicating a broader range of importance weights is beneficial. Smaller  $\alpha$  values improve performance while setting  $\alpha$  to 1 is suboptimal. This can be understood as it decreases the difference between high-frequency and low-frequency regions, as the weight for the latter one is set to 1. Additionally, a larger  $\theta$  (0.7 or 0.8) helps the model focus on important details.

#### 4.4. Visualizations

We visualize the reconstructed high-fidelity data conditioned on low-fidelity inputs in Figure 12 in Appendix E.3. PG-Diff consistently captures more fine-grained details, resulting in a closer resemblance to the high-fidelity ground truth compared to other methods. This is particularly evident in regions with complex vortical structures and turbulent features, where competing models often smooth out finer details. An example is the reconstructions from CNN and GAN on the *McWilliams FLOW* dataset. While direct mapping methods can achieve a low L2 norm, their reconstructed samples often merge small fine-grained regions into one large blurred region, leading to information loss and significant divergence from the high-fidelity data. By comparison, PG-Diff recovers the sharp edges, turbulence, and subtle variations in the flow field. We additionally show the strong reconstruction ability of our model variants compared to baselines in Appendix E.3. We also report the Learned Perceptual Image Patch Similarity (LPIPS) score (Zhang et al., 2018), Peak Signal-to-Noise Ratio (PSNR), and Structural Similarity Index Measure (SSIM) in Appendix E.4.

### 4.5. Physical Guidance

We conduct systematic study on how to schedule the residual correction during inference towards the best performance.

Schedule	$32 \times 32 \rightarrow 256 \times 256$		$64 \times 64 \rightarrow 256 \times 256$	
	L2	Res.	L2	Res.
Uniform 4	2.7910	26.32	1.6645	23.50
Start 3 End 1	2.7906	30.00	1.6617	32.51
Start 2 End 2	2.7897	40.12	1.6609	39.97
Start 1 End 3	2.7896	59.79	1.6617	59.39
Start 4 Space 1	<b>2.7889</b>	101.60	<b>1.6587</b>	105.84
Start 4 Space 2	<b>2.7888</b>	98.32	<b>1.6590</b>	102.14
Start 4 Space 3	<b>2.7887</b>	95.36	<b>1.6594</b>	95.08
End 4 Space 1	2.7930	<b>19.30</b>	1.6668	<b>21.97</b>
End 4 Space 2	2.7932	<b>17.55</b>	1.6747	<b>20.96</b>
End 4 Space 3	2.7924	<b>19.26</b>	1.6730	<b>23.57</b>

Table 2. Scheduling policy comparison on *Kolmogorov Flow*. Applying residual correction at the end leads to a reduced PDE residual, while placing it at the beginning achieves a lower L2 loss.

**Scheduling Policy.** We first explore the optimal schedule policy by comparing: 1.) *Uniform N*: Distributing N residual correction steps evenly across diffusion steps; 2.) *Start M, End N* Placing M consecutive correction steps at the start and N at the end of the diffusion process; 3.) *Start N, Space S*: Placing N correction steps at the start with a spacing of S; 4.) *End N, Space S*: Placing N correction steps at the end with a spacing of S. Results in Table 2 suggest that applying correction steps at the beginning achieves the lowest L2, while applying at the end has the lowest PDE residuals. To balance between L2 and PDE residual, we adopt the *Start N End N* schedule, which places N correction steps at both the beginning and the end of the diffusion process. We next study the optimal number of N.

**Number of Correction Steps.** We vary the number of N in the *Start N, End N* policy as shown in Figure 16 in Appendix E.5. We observe that increasing N leads to enhanced physical coherence measured by PDE residuals. However, L2 does not continuously decrease with larger N. It reaches a minimum when N = 2. This suggests that while more correction steps improve models’ adherence to physical laws, an excessive number may interfere with the model’s ability to accurately capture the intricate details of the turbulent flow. Therefore, we use *Start 2, End 2* as the optimal balance in our method.

### 4.6. Model Generalization

We observe that PG-Diff generalizes well to low-fidelity data generated with different solver configurations. We conduct evaluations over three generalization settings: time discretization, spatial domain size, and Reynolds number as shown in Table 3. We train PG-Diff on the original *Kolmogorov Flow* dataset, which has timestep  $dt = 1/32$ ,

Variation	Model	L2	Res.
<b>Time Discretization Variations</b>			
$dt = 1/40$	Trained on Original Data	2.8144	34.29
	Trained on $dt = 1/40$ Data	2.8136	34.52
$dt = 1/50$	Trained on Original Data	2.7761	37.11
	Trained on $dt = 1/50$ Data	2.7795	30.60
<b>Spatial Domain Size Variations</b>			
$1\pi \times 1\pi$	Trained on Original Data	1.9045	262.42
	Trained on $1\pi \times 1\pi$ Data	1.7672	190.99
$1.5\pi \times 1.5\pi$	Trained on Original Data	2.3573	80.66
	Trained on $1.5\pi \times 1.5\pi$ Data	2.3028	88.88
<b>Reynolds Number Variations</b>			
$Re = 500$	Trained on Original Data	2.3694	24.11
	Trained on $Re = 500$ Data	2.3542	26.96
$Re = 2000$	Trained on Original Data	3.2957	23.84
	Trained on $Re = 2000$ Data	3.2914	22.48

Table 3. Generalization results on *Kolmogorov Flow* dataset with  $32 \times 32 \rightarrow 256 \times 256$  setting.

spatial domain size  $2\pi \times 2\pi$ , and Reynolds number  $Re = 1000$ . We then directly test these new low-fidelity data on the trained model, without any additional retraining or fine-tuning. We compare the performance against models directly trained one each new configuration.

The results reveal that the pertained PG-Diff performs comparably to trained ones directly on each new configuration. This underscores our model’s strong generalization capabilities across different solver configurations. Such generalization ability is particularly important given the high-level objective is to combine PG-Diff with solvers operating on coarser grids to generate high-fidelity data faster. The generalization ability can due to the fact that both our *importance weight* mechanism and *residual correction* modules are training-free. They enable our model to locate fine-grained high-fidelity details and adhere to physical laws independent of training data. A similar trend is also observed in  $4 \times$  upsampling experiments, shown in Appendix E.7.

## 5. Conclusion

We study a novel problem of reconstructing high-fidelity CFD from solver-generated low-fidelity inputs. Our diffusion model, PG-Diff, achieves high-quality reconstruction guided by *Importance Weight* and *Residual Correction*. Although the proposed diffusion framework achieves a significant speedup compared to high-fidelity solvers, it remains relatively slow compared to direct mapping models. Future work could explore recent advancements in accelerating diffusion sampling, such as Lu et al. (2022), to further enhance the efficiency of the reconstruction process.

## 6. Impact Statement

This paper presents work whose goal is to advance the field of Machine Learning. There are many potential societal consequences of our work, none which we feel must be specifically highlighted here.

## 7. Impact Statement

This work was partially supported by NSF 2211557, NSF 2119643, NSF 2303037, NSF 2312501, NSF 2200274, NSF 2106859, NIH U54HG012517, NIH U24DK097771, SRC JUMP 2.0 Center, Amazon Research Awards, Snapchat Gifts, and Optum AI.

## References

- Akansu, A. N. and Haddad, R. A. *Multiresolution Signal Decomposition: Transforms, Subbands, and Wavelets*. Academic Press, San Diego, CA, 1992.
- Bai, X., Wang, Y., and Zhang, W. Applying physics informed neural network for flow data assimilation. *Journal of Hydrodynamics*, 32:1050–1058, 2020. doi: 10.1007/s42241-020-0077-2.
- Chen, Z., Liu, Y., and Sun, H. Physics-informed learning of governing equations from scarce data. *Nature Communications*, 12:6136, 2021. doi: 10.1038/s41467-021-26434-1.
- Chung, H., Kim, J., Mccann, M. T., Klasky, M. L., and Ye, J. C. Diffusion posterior sampling for general noisy inverse problems. In *The Eleventh International Conference on Learning Representations*, 2023. URL <https://openreview.net/forum?id=OnD9zGAGT0k>.
- Daubechies, I. *Ten Lectures on Wavelets*. Society for Industrial and Applied Mathematics, 1992a. doi: 10.1137/1.9781611970104. URL <https://epubs.siam.org/doi/abs/10.1137/1.9781611970104>.
- Daubechies, I. *Ten Lectures on Wavelets*. SIAM, Philadelphia, PA, 1992b.
- Fu, C., Helwig, J., and Ji, S. Semi-supervised learning for high-fidelity fluid flow reconstruction. In *The Second Learning on Graphs Conference*, 2023. URL <https://openreview.net/forum?id=695IYJh1Ba>.
- Fukami, K., Fukagata, K., and Taira, K. Super-resolution reconstruction of turbulent flows with machine learning. *Journal of Fluid Mechanics*, 870:106–120, 2019. doi: 10.1017/jfm.2019.238.
- Fukami, K., Maulik, R., Ramachandra, N., Fukagata, K., and Taira, K. Global field reconstruction from sparse sensors with voronoi tessellation-assisted deep learning. *Nature Machine Intelligence*, 3(11):945–951, November 2021. ISSN 2522-5839. doi: 10.1038/s42256-021-00402-2. Publisher Copyright: © 2021, The Author(s), under exclusive licence to Springer Nature Limited.
- Gao, H., Sun, L., and Wang, J.-X. Super-resolution and denoising of fluid flow using physics-informed convolutional neural networks without high-resolution labels. *Physics of Fluids*, 33(7):073603, 2021. doi: <https://doi.org/10.1063/5.0054312>.
- Gonzalez, R. C. and Woods, R. E. *Digital Image Processing*. Prentice Hall, Upper Saddle River, NJ, USA, 3rd edition, 2007.
- Ho, J., Jain, A., and Abbeel, P. Denoising diffusion probabilistic models. *arXiv preprint arxiv:2006.11239*, 2020.
- Huang, J., Yang, G., Wang, Z., and Park, J. J. Diffusionpde: Generative pde-solving under partial observation, 2024. URL <https://arxiv.org/abs/2406.17763>.
- Huang, Z., Sun, Y., and Wang, W. Generalizing graph ode for learning complex system dynamics across environments. In *Proceedings of the 29th ACM SIGKDD Conference on Knowledge Discovery and Data Mining*, pp. 798–809, 2023.
- Jiang, C. M., Esmaeilzadeh, S., Azzadenesheli, K., Kashinath, K., Mustafa, M. A., Tchelepi, H. A., Marcus, P. S., Prabhat, and Anandkumar, A. Mesh-freeflownet: A physics-constrained deep continuous space-time super-resolution framework. *SC20: International Conference for High Performance Computing, Networking, Storage and Analysis*, pp. 1–15, 2020. URL <https://api.semanticscholar.org/CorpusID:218487006>.
- Kingma, D. P. and Ba, J. Adam: A method for stochastic optimization. *International Conference on Learning Representations (ICLR)*, 2015. URL <https://arxiv.org/abs/1412.6980>.
- Ledig, C., Theis, L., Huszár, F., Caballero, J., Aitken, A. P., Tejani, A., Totz, J., Wang, Z., and Shi, W. Photo-realistic single image super-resolution using a generative adversarial network. *2017 IEEE Conference on Computer Vision and Pattern Recognition (CVPR)*, pp. 105–114, 2016. URL <https://api.semanticscholar.org/CorpusID:211227>.
- Li, M. and McComb, C. Using Physics-Informed Generative Adversarial Networks to Perform Super-Resolution for Multiphase Fluid Simulations. *Journal of Computing and Information Science in Engineering*, 22(4):044501, 02

2022. ISSN 1530-9827. doi: 10.1115/1.4053671. URL <https://doi.org/10.1115/1.4053671>.
- Li, Z.-Y., Kovachki, N. B., Azizzadenesheli, K., Liu, B., Bhattacharya, K., Stuart, A. M., and Anandkumar, A. Fourier neural operator for parametric partial differential equations. *ArXiv*, abs/2010.08895, 2020. URL <https://api.semanticscholar.org/CorpusID:224705257>.
- Li, Z.-Y., Zheng, H., Kovachki, N. B., Jin, D., Chen, H., Liu, B., Azizzadenesheli, K., and Anandkumar, A. Physics-informed neural operator for learning partial differential equations. *ArXiv*, abs/2111.03794, 2021. URL <https://api.semanticscholar.org/CorpusID:243847513>.
- Lu, C., Zhou, Y., Bao, F., Chen, J., Li, C., and Zhu, J. Dpm-solver: A fast ode solver for diffusion probabilistic model sampling in around 10 steps. *arXiv preprint arXiv:2206.00927*, 2022.
- Lugmayr, A., Danelljan, M., Van Gool, L., and Timofte, R. SrfLOW: Learning the super-resolution space with normalizing flow. In *ECCV*, 2020.
- McWilliams, J. C. The emergence of isolated coherent vortices in turbulent flow. *Journal of Fluid Mechanics*, 146:21–43, 1984. doi: 10.1017/S0022112084001750.
- Meng, C., He, Y., Song, Y., Song, J., Wu, J., Zhu, J.-Y., and Ermon, S. SDEdit: Guided image synthesis and editing with stochastic differential equations. In *International Conference on Learning Representations*, 2022.
- Navier, C. L. M. H. Mémoire sur les lois du mouvement des fluides. *Mémoires de l'Académie Royale des Sciences de l'Institut de France*, 6:389–440, 1823.
- Orszag, S. A. Comparison of pseudospectral and spectral approximation. *Studies in Applied Mathematics*, 51(3):253–259, September 1972. doi: 10.1002/sapm1972513253.
- Pradhan, A. and Duraisamy, K. Variational multi-scale super-resolution: A data-driven approach for reconstruction and predictive modeling of unresolved physics, 2021. URL <https://arxiv.org/abs/2101.09839>.
- Qiu, J., Huang, J., Zhang, X., Lin, Z., Pan, M., Liu, Z., and Miao, F. Pi-fusion: Physics-informed diffusion model for learning fluid dynamics, 2024. URL <https://arxiv.org/abs/2406.03711>.
- Raissi, M., Perdikaris, P., and Karniadakis, G. Physics-informed neural networks: A deep learning framework for solving forward and inverse problems involving nonlinear partial differential equations. *Journal of Computational Physics*, 378:686–707, 2019. ISSN 0021-9991. doi: <https://doi.org/10.1016/j.jcp.2018.10.045>. URL <https://www.sciencedirect.com/science/article/pii/S0021999118307125>.
- Ren, P., Rao, C., Liu, Y., Ma, Z., Wang, Q., Wang, J.-X., and Sun, H. Physr: Physics-informed deep super-resolution for spatiotemporal data. *Journal of Computational Physics*, 492:112438, 2023. ISSN 0021-9991. doi: <https://doi.org/10.1016/j.jcp.2023.112438>. URL <https://www.sciencedirect.com/science/article/pii/S0021999123005338>.
- Saharia, C., Ho, J., Chan, W., Salimans, T., Fleet, D. J., and Norouzi, M. Image super-resolution via iterative refinement. *arXiv:2104.07636*, 2021.
- Sanchez-Gonzalez, A., Godwin, J., Pfaff, T., Ying, R., Leskovec, J., and Battaglia, P. Learning to simulate complex physics with graph networks. In III, H. D. and Singh, A. (eds.), *Proceedings of the 37th International Conference on Machine Learning*, volume 119 of *Proceedings of Machine Learning Research*, pp. 8459–8468. PMLR, 13–18 Jul 2020. URL <https://proceedings.mlr.press/v119/sanchez-gonzalez20a.html>.
- Sarkar, R. K., Majumdar, R., Jadhav, V., Sakhinana, S. S., and Runkana, V. Redefining super-resolution: Fine-mesh pde predictions without classical simulations, 2023. URL <https://arxiv.org/abs/2311.09740>.
- Shu, D., Li, Z., and Farimani, A. B. A physics-informed diffusion model for high-fidelity flow field reconstruction. *Journal of Computational Physics*, pp. 111972, 2023.
- Shysheya, A., Diaconu, C., Bergamin, F., Perdikaris, P., Hernández-Lobato, J. M., Turner, R. E., and Mathieu, E. On conditional diffusion models for pde simulations. In *The Thirty-eighth Annual Conference on Neural Information Processing Systems*, 2024. URL <https://openreview.net/forum?id=nQ18EjyMzh>.
- Song, J., Meng, C., and Ermon, S. Denoising diffusion implicit models. *arXiv:2010.02502*, October 2020. URL <https://arxiv.org/abs/2010.02502>.
- Wang, H., Cao, Y., Huang, Z., Liu, Y., Hu, P., Luo, X., Song, Z., Zhao, W., Liu, J., Sun, J., et al. Recent advances on machine learning for computational fluid dynamics: A survey. *arXiv preprint arXiv:2408.12171*, 2024.
- Wang, X., Yu, K., Wu, S., Gu, J., Liu, Y., Dong, C., Qiao, Y., and Loy, C. C. Esrgan: Enhanced super-resolution generative adversarial networks. In Leal-Taixé, L. and Roth, S. (eds.), *Computer Vision – ECCV 2018 Workshops*, pp. 63–79, Cham, 2019. Springer International Publishing. ISBN 978-3-030-11021-5.

- Yang, G. and Sommer, S. A denoising diffusion model for fluid field prediction, 2023. URL <https://arxiv.org/abs/2301.11661>.
- Yang, L. and Hong, S. Unsupervised time-series representation learning with iterative bilinear temporal-spectral fusion. 07 2022.
- Yu, S., Tack, J., Mo, S., Kim, H., Kim, J., Ha, J.-W., and Shin, J. Generating videos with dynamics-aware implicit generative adversarial networks. In *International Conference on Learning Representations*, 2022.
- Zeng, X., Vahdat, A., Williams, F., Gojcic, Z., Litany, O., Fidler, S., and Kreis, K. Lion: Latent point diffusion models for 3d shape generation. In *Advances in Neural Information Processing Systems (NeurIPS)*, 2022.
- Zhang, R., Isola, P., Efros, A. A., Shechtman, E., and Wang, O. The unreasonable effectiveness of deep features as a perceptual metric. In *Proceedings of the IEEE Conference on Computer Vision and Pattern Recognition (CVPR)*, pp. 586–595, 2018.
- Zhang, Y., Zhang, D., and Jiang, H. Review of challenges and opportunities in turbulence modeling: A comparative analysis of data-driven machine learning approaches. *Journal of Marine Science and Engineering*, 11(7):1440, 2023.
- Zhou, L., Du, Y., and Wu, J. 3d shape generation and completion through point-voxel diffusion. In *Proceedings of the IEEE/CVF International Conference on Computer Vision (ICCV)*, pp. 5826–5835, October 2021.
- Zhu, Y., Zhang, K., Liang, J., Cao, J., Wen, B., Timofte, R., and Gool, L. V. Denoising diffusion models for plug-and-play image restoration. In *IEEE Conference on Computer Vision and Pattern Recognition Workshops (NTIRE)*, 2023.

## Contents

### A. Limitations

Our current research on super-resolution in computational fluid dynamics (CFD) focuses exclusively on vorticity data. However, future work can broaden its scope to include the reconstruction of high-fidelity velocity and pressure fields. These additional physical quantities are critical for capturing a more comprehensive representation of fluid dynamics.

### B. Broader Impacts

By enhancing the accuracy of CFD simulations, this approach can significantly reduce the computational costs associated with high-resolution simulations, which are often prohibitively expensive in terms of both time and resources. This has implications for a wide range of industries, including aerospace, automotive design, and environmental engineering, where high-fidelity simulations are essential for optimizing performance, safety, and sustainability. Additionally, by improving the quality of low-resolution CFD data, our work could enable more accessible, efficient research and development processes, allowing smaller organizations and research teams to leverage advanced simulation capabilities.

### C. Model Details

#### C.1. Discrete Wavelet Transformation

The Discrete Wavelet Transform (DWT) decomposes an image  $I \in \mathbb{R}^{n \times n}$  into different frequency components by successively applying low-pass and high-pass filters. Given an image  $I$ , the DWT first applies a low-pass filter  $g[n]$  and a high-pass filter  $h[n]$  along each row, producing two sub-bands:  $I_{\text{low}}[i, j] = \sum_k I[i, k] \cdot g[2j - k]$  and  $I_{\text{high}}[i, j] = \sum_k I[i, k] \cdot h[2j - k]$ , each downsampled by a factor of 2 along the columns, resulting in matrices of shape  $n \times \frac{n}{2}$ .

Next, the same filters are applied to each column of  $I_{\text{low}}$  and  $I_{\text{high}}$ , generating four sub-bands:

$$\begin{aligned} LL[i, j] &= \sum_k I_{\text{low}}[k, j] \cdot g[2i - k] \\ LH[i, j] &= \sum_k I_{\text{low}}[k, j] \cdot h[2i - k], \\ HL[i, j] &= \sum_k I_{\text{high}}[k, j] \cdot g[2i - k] \\ HH[i, j] &= \sum_k I_{\text{high}}[k, j] \cdot h[2i - k]. \end{aligned}$$

The resulting sub-bands  $LL$ ,  $LH$ ,  $HL$ , and  $HH$  each have dimensions  $\frac{n}{2} \times \frac{n}{2}$ , capturing the low-low, low-high, high-

low, and high-high frequency components, respectively, of the original image.

- $LL$ : This sub-band captures the approximation or low-frequency content of the image in both the horizontal and vertical directions. It retains most of the important structural information of the image.
- $LH$ : This sub-band captures the vertical high-frequency components (edges and fine details) of the image. It primarily highlights vertical details like vertical edges.
- $HL$ : This sub-band captures the horizontal high-frequency components of the image. It emphasizes horizontal edges or features.
- $HH$ : This sub-band captures the high-frequency content in both horizontal and vertical directions, corresponding to diagonal details such as corners, intersections, and textures.

These sub-bands collectively represent the image in both spatial and frequency domains. Higher values in the  $LH$ ,  $HL$ , and  $HH$  sub-bands correspond to regions with higher frequency variations (such as edges or fine details) in the respective subdomains. Higher values in the  $LL$  sub-band correspond to regions with higher intensity or brightness in the original image but represent low-frequency content.

#### C.2. Implementation Details

We implement all models in PyTorch and show their implementation details below.

**Bicubic** Bicubic interpolation is a widely used image scaling technique that enhances the resolution of low-resolution images by using a weighted average of pixels in a 4x4 neighborhood around each pixel. Bicubic interpolation uses 16 neighboring pixels to produce smoother and more accurate results. This method is deterministic and does not involve any machine learning or training.

**CNN** We modify the hybrid Downsampled Skip-Connection Multi-Scale (DSC/MS) architecture proposed by Fukami et al. (2019). In the original implementation of the DSC/MS model, the model operates on a single frame of velocity field. We modify the model to work in our settings, where the input consists of three consecutive frames of low-fidelity vorticity data, upsampled to  $256 \times 256$ . The DSC component starts by compressing the input through a series of convolutional layers, effectively capturing multi-scale features. Skip connections are then introduced at various stages to preserve spatial information, ensuring that the network retains fine details from earlier layers. The MS component consists of three parallel convolutional paths that capture

features at different scales and combine them to produce the high-resolution output of three consecutive frames of  $256 \times 256$  vorticity data. The training process uses the L2 loss function, running for 300 epochs with a learning rate of  $1e - 5$ .

**GAN** We modify the physics-informed GAN proposed by Li & McComb (2022). In the original implementation of the physics-informed GAN, the input was low-resolution phase fraction data from a multiphase fluid simulation, and the output was a high-resolution phase fraction representation. Our adaptation uses low-fidelity vorticity data upsampled to  $256 \times 256$  as input and high-fidelity vorticity data as output. The generator consisted of multiple convolutional layers and residual blocks, while the discriminator had a series of convolutional layers followed by dense layers. The physics-informed loss function combined a mean squared error (MSE) term with an additional term designed to enforce conservation of mass, ensuring the generated data remained consistent with fluid dynamics principles. The model was trained for 300 epochs with a learning rate of  $1e - 5$ .

**Diffusion** The unconditional diffusion model in Shu et al. (2023) is trained only on high-fidelity CFD data without requiring low-fidelity data during training. The model uses a U-Net architecture with hierarchical convolutional blocks, multi-level skip connections, and a self-attention mechanism in the bottleneck layer to capture complex features of the high-fidelity data. The training process spans 300 epochs, where the model learns to predict and remove noise added during the forward diffusion process. During inference, the model starts with a guided reverse diffusion process from an intermediate timestep  $t < T$  instead of starting with complete random Gaussian noise. The low-fidelity input data is first upsampled to the target resolution and then combined with Gaussian noise to form the initial input for the reverse diffusion process. This noisy data serves as guidance for generating the high-fidelity output.

**Conditional Diffusion** The conditional diffusion model proposed in Shu et al. (2023) incorporates physics-informed guidance during both training and inference by utilizing the gradient of the PDE residual with respect to the noised sample. During training, at each step of the forward diffusion process, the residual of the governing PDE is computed based on the current noised sample. The gradient of this residual is calculated and concatenated with the noised sample as input to the U-Net. During inference, the same process is applied: the model computes the gradient of the PDE residual at each reverse diffusion step and concatenates it with the noised sample.

**PG-Diff** Starting with  $x_t$ , which represents an intermediate denoised state at time-step  $t$ , the denoising process utilizes a U-Net model to estimate  $\epsilon_\theta$ . The UNet architecture starts with an initial 3x3 convolution that maps

the `in_channels:3` to `ch:128`. The encoder progressively downsamples at each level, using a channel multiplier `ch_mult:[1, 1, 1, 2]`, which means the channels stay at 128 for three levels and then double to 256. Attention blocks are applied at resolutions to capture long-range dependencies. The decoder mirrors the encoder, using up-sampling layers to restore spatial resolution and skip connections to preserve details. The output is transformed back to the original `out_ch:3` channels through a final 3x3 convolution. The estimated  $\epsilon_\theta$  is then integrated into a sampling process, outlined in detail by Steps 5 of Algorithm 1, to iteratively generate  $x_{t-1}$ . In this approach, the inference phase is governed by several critical hyperparameters:  $t$ , which defines where the partial backward diffusion sampling begins;  $K$ , the total number of DDIM backward diffusion steps performed; and the set  $\{\beta_t\}_{t=1}^T$ , which dictates the scaling factors controlling noise variance throughout the forward diffusion stages. We adopt the same hyperparameters used in Shu et al. (2023). The training algorithm for our PG-Diff is presented in Algorithm 2. The PG-Diff training procedure involves iteratively updating the denoiser  $\epsilon_\theta$  using high-fidelity training data  $\mathcal{Y}^{\text{train}}$ . In each training iteration, a sample  $y$  is drawn from the high-fidelity training dataset, and a time-step  $t$  is randomly selected from a uniform distribution over  $\{1, \dots, T\}$ . Gaussian noise  $\epsilon_t$  is then sampled from  $\mathcal{N}(0, I)$ . The high-fidelity data  $y$  is transformed into the wavelet domain to compute an importance weight  $a$ . The model’s parameters  $\theta$  are updated through a gradient descent step using the gradient  $\nabla_{\theta} a \odot \|\epsilon_t - \epsilon_\theta(\sqrt{\alpha_t}y + \sqrt{1 - \alpha_t}\epsilon_t, t)\|^2$ . This process repeats until the model converges, enabling the denoiser to learn to reconstruct fine-grained details in the high-fidelity data effectively.

---

**Algorithm 2** PG-Diff Model Training.

---

**Require:**  $\mathcal{Y}^{\text{train}} \sim p_{\mathcal{Y}}^{\text{train}}$  (High-fidelity data used for training),  $\epsilon_\theta$  (Denoiser to be trained)

- 1: **repeat**
- 2:    $y \in \mathcal{Y}^{\text{train}}$
- 3:    $t \sim \text{Uniform}(\{1, \dots, T\})$
- 4:    $\epsilon_t \sim \mathcal{N}(0, I)$
- 5:   Transform  $y$  into the wavelet domain and compute the importance weight  $a$
- 6:   Take a step of gradient descent on  $\theta$  with the following gradient:

$$\nabla_{\theta} a \odot \|\epsilon_t - \epsilon_\theta(\sqrt{\alpha_t}y + \sqrt{1 - \alpha_t}\epsilon_t, t)\|^2$$

- 7: **until** converged
-

## D. Dataset

All datasets are generated using pseudo-spectral solver implemented by Li et al. (2020). Our dataset will be released upon publication of our paper and be free to use.

The time-stepping method employed is a combination of the Crank-Nicholson scheme and Heun’s method. The Crank-Nicholson scheme is an implicit, second-order accurate method, and it is applied to the viscous term. This allows the solver to be stable even for relatively large time steps when handling viscous diffusion. Heun’s method, a second-order Runge-Kutta technique, is used to handle the non-linear advection term. The combination of these two methods provides an efficient and accurate way to evolve the vorticity field over time, with the implicit Crank-Nicholson step ensuring stability for stiff viscous terms, and Heun’s method capturing the non-linearity of the advection.

For numerical stability, the solver uses an adaptive time-stepping approach governed by the Courant-Friedrichs-Lewy (CFL) condition. The CFL condition ensures that the time step remains sufficiently small relative to the velocity field and the external forcing, preventing instabilities that can arise from rapid changes in the solution. Additionally, the dealiasing procedure, using the 2/3 rule, removes high-frequency components from the Fourier spectrum, ensuring that non-physical aliasing effects are avoided.

---

### Algorithm 3 Pseudo-spectral Navier-Stokes Solver

---

- 1: **Input:** Initial vorticity  $\omega_0$ , forcing  $f$ , Reynolds number  $Re$ , total time  $T$ , timestep  $\Delta t$ , domain size  $L_1, L_2$ , grid size  $s_1, s_2$ , adaptivity flag
  - 2: **Output:** Vorticity  $\omega$  at time  $T$
  - 3: **Initialize:** Compute wavenumbers, Laplacian, and dealiasing mask
  - 4:
  - 5: **while**  $t < T$  **do**
  - 6:   **if** adaptive **then**
  - 7:     Compute velocity field  $\mathbf{u} = \nabla^\perp \psi$
  - 8:     Update timestep  $\Delta t$  based on CFL
  - 9:   **end if**
  - 10:   Compute non-linear term in Fourier space
  - 11:   Predictor and corrector steps using Crank-Nicholson + Heun
  - 12:   Apply dealiasing mask
  - 13:   Update time  $t = t + \Delta t$
  - 14: **end while**
  - 15: Return Vorticity  $\omega$
- 

**Taylor Green Vortex** The initial vorticity field is based on the analytical solution of the TGV, and to generate different trajectories, we added random perturbations from a Gaussian random field. These perturbations introduce variability to the initial conditions while maintaining the

overall vortex structure. No external forcing was applied during the simulation, and the spatial domain is  $[0, \frac{3}{2}\pi]^2$  with a fixed Reynolds number of 1000. The simulation used a time step  $dt = \frac{1}{32}$ , and 100 trajectories were generated each with a total duration of  $T = 6$  seconds. The initial vorticity field is based on the analytical solution for the two-dimensional periodic domain. The vorticity field  $\omega$  is initialized as  $\omega = -2U_0 k \sin(kx) \sin(ky)$ , where  $U_0$  is the initial velocity amplitude, and  $k$  is the wave number that determines the size of the vortices. To introduce variability and generate different trajectories, a Gaussian Random Field is added as a perturbation to the initial vorticity.

**Decaying Turbulence** The spatial domain is  $[0, 1]^2$ , with periodic boundary conditions and a fixed Reynolds number of 450. The simulation used a time step  $dt = \frac{1}{32}$ , and 400 trajectories were generated, each with a total duration of  $T = 2$  seconds. The initial conditions for the decaying turbulence dataset are generated by superimposing randomly positioned vortices of varying intensity and size. Each vortex is characterized by a randomly selected core size and maximum rotational velocity, allowing for a diverse range of initial flow structures. The vortices are distributed randomly throughout the domain, and their periodic images are added to ensure the proper enforcement of periodic boundary conditions.

**Kolmogorov Flow** The initial vorticity field is generated using a Gaussian random field, and the system is subjected to a forcing term of the form  $f(\mathbf{x}) = -4 \cos(4x_2) - 0.1\omega(\mathbf{x}, t)$ . This forcing drives the flow in the y-direction while introducing a drag force that dissipates energy. The spatial domain is  $[0, 2\pi]^2$ , with a fixed Reynolds number of 1000. The simulation used a time step  $dt = \frac{1}{32}$ , and 50 trajectories were generated, each with a total duration of  $T = 10$  seconds. The initial vorticity field is produced by sampling from a Gaussian Random Field. As the external forcing continually adds energy to the system, the initially simple vorticity evolves into intricate and turbulent structures. The vorticity is allowed to evolve over a 5-second period, and the final state at the end of this interval is used as the initial condition for our dataset.

**McWilliams Flow** The phenomenon illustrates the emergence of order from initially disordered turbulent motion, driven by viscous dissipation and the self-organization of the flow. No external forcing is applied during the simulation, allowing for a natural decay and evolution of the turbulence. The spatial domain is  $[0, 2\pi]^2$ , with periodic boundary conditions and a Reynolds number of 2000, providing a high degree of turbulence. The simulation used a time step  $dt = \frac{1}{32}$ , and 50 trajectories were generated, each with a total duration of  $T = 10$  seconds. The initial vorticity field for the *McWilliams Flow* is generated following the method described by McWilliams (1984). The process

begins by constructing a Fourier mesh over the spatial domain, where the wavenumbers  $k_x$  and  $k_y$  are calculated. A scalar wavenumber function is prescribed, and the ensemble variance is determined to ensure that the energy distribution in Fourier space follows the desired spectral shape. Random Gaussian perturbations are applied to each Fourier component of the stream function, producing a random realization of the vorticity field. To ensure the stream function has a zero mean, a spectral filter is applied, and the field is normalized based on the kinetic energy. Finally, the vorticity field is computed in physical space by taking the inverse Laplacian of the stream function in Fourier space, resulting in a turbulent flow field that evolves naturally without external forcing.

	Kolmogorov Flow	McWilliams Flow	Taylor Green Vortex	Decaying Turbulence
Res.	44.13	6.64	5101.65	212.43

Table 4. Residual of high-fidelity samples for each dataset.

We show the visualization of the four datasets below.

### D.1. Residual Calculation

The PDE residual of the governing equation  $\mathcal{R}(\omega)$  is defined as

$$\mathcal{R}(\omega) = \frac{1}{N} \sum_{i,j} [\text{LHS}(\omega)_{i,j} - \text{RHS}(\omega)_{i,j}]^2$$

where  $\text{LHS}(\omega)$  and  $\text{RHS}(\omega)$  represent the left-hand side and right-hand side expressions of the PDE, respectively.  $\omega$  represents the vorticity.  $N$  represents the number of grid points. For the incompressible Navier-Stokes equation tested in this paper, the residual is defined as

$$\mathcal{R}(\omega) = \frac{1}{N} \sum_{i,j} \left[ \frac{\partial \omega(\mathbf{x}, t)}{\partial t} + \mathbf{u}(\mathbf{x}, t) \cdot \nabla \omega(\mathbf{x}, t) - \frac{1}{Re} \nabla^2 \omega(\mathbf{x}, t) - f(\mathbf{x}) \right]^2$$

## E. Additional Experimental Results

### E.1. DWT visualization

Figure 7 presents sample importance masks identified as high-frequency features using the DWT. These masks highlight the regions where our model focuses to capture intricate details. The samples clearly demonstrate that our method effectively captures the fine-grained structures in the turbulent flow, validating its ability to reconstruct small-scale vortices and turbulence that are often missed by conventional approaches.

### E.2. Multi-Scale Evaluation

To comprehensively evaluate the model’s ability to capture both overall flow dynamics and intricate details, we performed a multi-scale analysis by transforming the predicted and ground truth flow fields into the wavelet domain. This transformation produced four subdomains: LL (low-low), LH (low-high), HL (high-low), and HH (high-high). The LL subdomain represents broad, low-frequency components, while the LH, HL, and HH subdomains capture increasingly finer, high-frequency features, including turbulent structures. We then assessed the L2 norm across these subdomains to gain deeper insights into the model’s effectiveness in reconstructing both large-scale patterns and fine-grained details.

### E.3. Reconstruction Visualization

We present visualizations of the reconstructed high-fidelity data using PG-Diffw/o Cor across different methods and datasets. As shown in Figure 13 and Figure 14, PG-Diff consistently produces impressive qualitative results.

### E.4. LPIPS Scores

Direct mapping models are effective at minimizing L2 loss. However, these models tend to produce samples that appear smooth and blurry, often missing the intricate details. This is because the L2 loss emphasizes pixel-wise accuracy, which can lead to averaging effects and the loss of fine-grained details. To address this issue, we use the LPIPS (Learned Perceptual Image Patch Similarity) metric, which focuses on perceptual differences and provides a more qualitative assessment of the reconstructed flow fields, capturing the texture and small-scale structures. The results are presented in Table 5

Although LPIPS is trained on the ImageNet dataset, which consists of natural images, it remains a valuable metric for evaluating perceptual quality in CFD applications. This is because LPIPS leverages features from deep neural networks that are effective at capturing multi-scale patterns, textures, and perceptual similarities, regardless of the specific domain. Fluid dynamics data often have complex structures and turbulent patterns that share characteristics with textures found in natural images, making LPIPS suitable for assessing the fidelity of reconstructed flow fields. Thus, despite being trained on ImageNet, LPIPS can still effectively quantify how well the reconstructed samples retain important perceptual details, making it a robust metric for evaluating the visual quality of CFD reconstructions.

### E.5. Importance Weight Sensitivity Analysis

We present a sensitivity analysis to explore how different hyperparameter settings affect the performance of the Importance Weight Strategy. The importance weight strategy

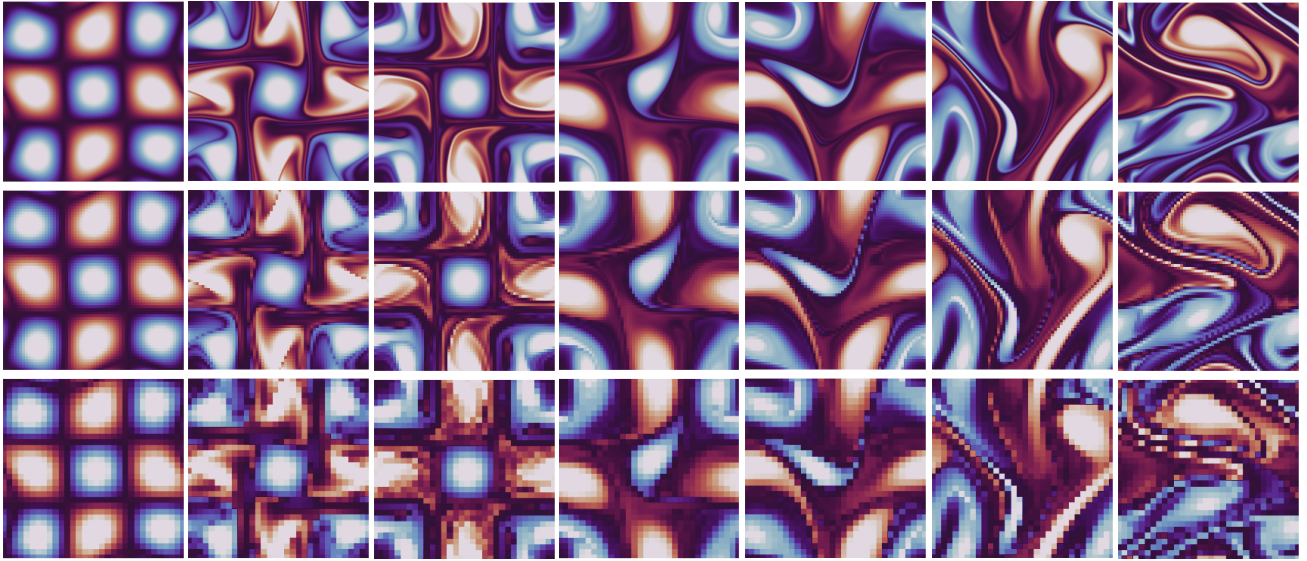


Figure 3. Example trajectory of the Taylor Green Vortex dataset. The first row is the high-fidelity data with  $256 \times 256$  discretization grid. The second and third rows are low fidelity data with  $64 \times 64$  and  $32 \times 32$  discretization grids, respectively. For visualization, we upsample the low-fidelity data to  $256 \times 256$  discretization grid.

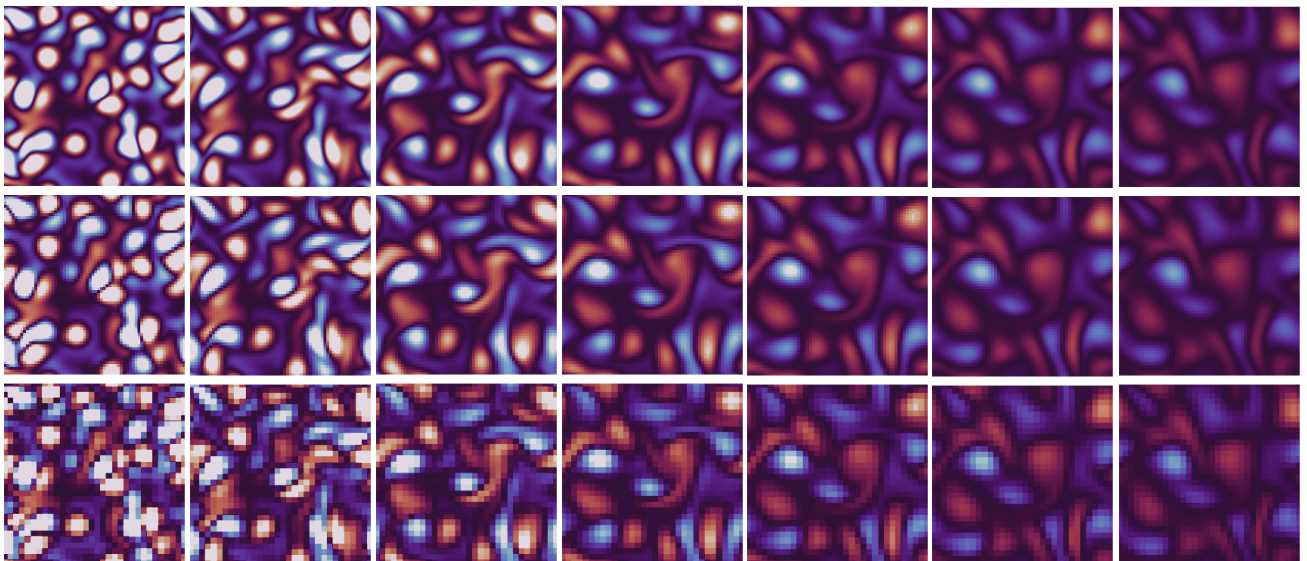


Figure 4. Example trajectory of the Decaying Turbulence dataset. The first row is the high-fidelity data with  $256 \times 256$  discretization grid. The second and third rows are low fidelity data with  $64 \times 64$  and  $32 \times 32$  discretization grids, respectively. For visualization, we upsample the low-fidelity data to  $256 \times 256$  discretization grid.

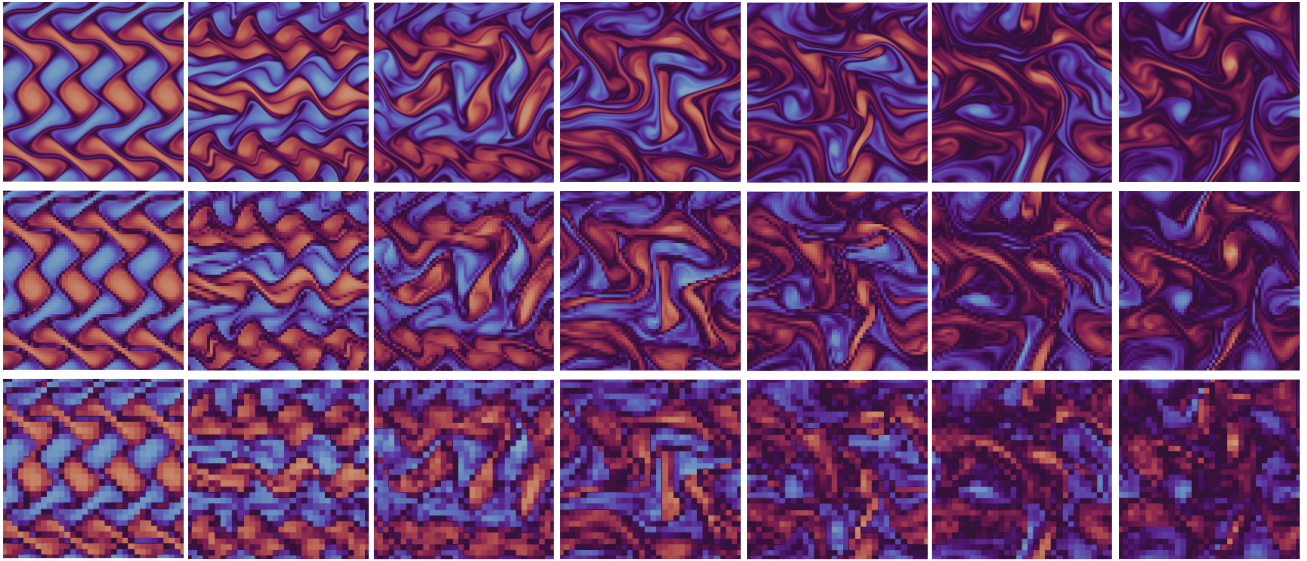


Figure 5. Example trajectory of the *Kolmogorov Flow* dataset. The first row is the high-fidelity data with  $256 \times 256$  discretization grid. The second and third rows are low fidelity data with  $64 \times 64$  and  $32 \times 32$  discretization grids, respectively. For visualization, we upsample the low-fidelity data to  $256 \times 256$  discretization grid.

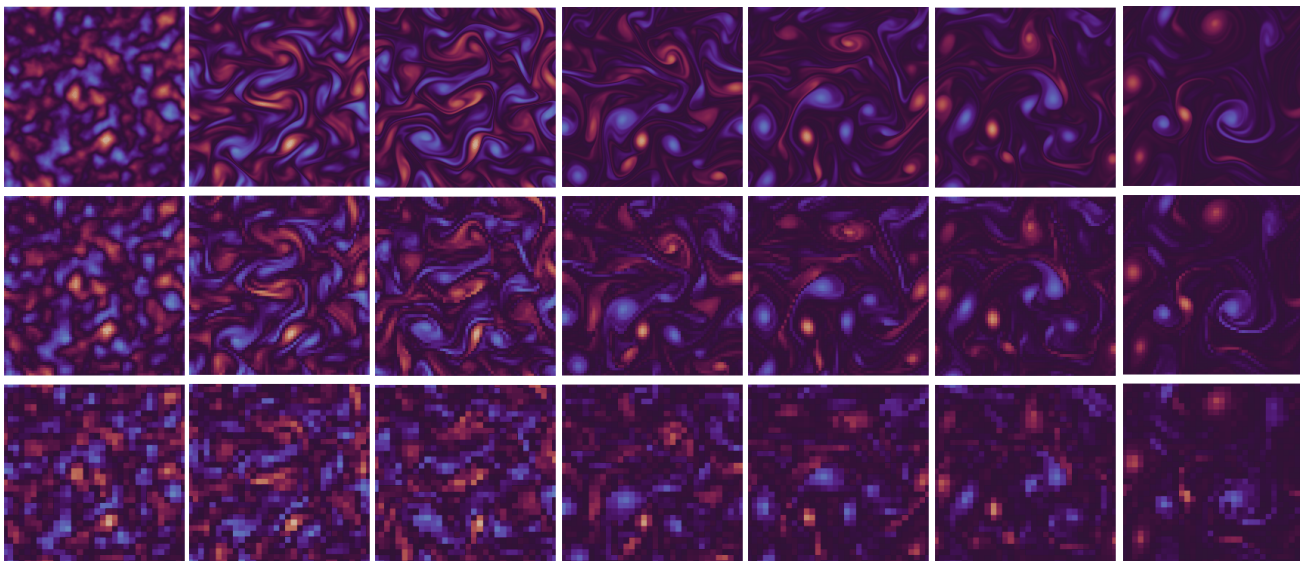


Figure 6. Example trajectory of the *McWilliams Flow* dataset. The first row is the high-fidelity data with  $256 \times 256$  discretization grid. The second and third rows are low fidelity data with  $64 \times 64$  and  $32 \times 32$  discretization grids, respectively. For visualization, we upsample the low-fidelity data to  $256 \times 256$  discretization grid.

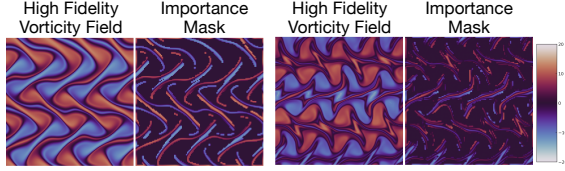


Figure 7. High frequency components in the *Kolmogorov Flow* field identified by discrete wavelet transformation. We compare the high fidelity vorticity field with the importance mask.

	Bicubic	CNN	GAN	Diff	Cond Diff	PG-Diff
<i>Kolmogorov Flow</i>	0.5421	0.5358	0.5109	0.2848	0.2869	0.2781
	0.2919	0.4065	0.4082	0.1215	0.1229	0.1097
<i>McWilliams Flow</i>	0.5736	0.4921	0.4505	0.3524	0.3540	0.2936
	0.3417	0.3948	0.3948	0.1457	0.1604	0.1298
<i>Decaying Turbulence</i>	0.2221	0.1448	0.1991	0.4215	0.1688	0.1397
	0.0794	0.1521	0.1407	0.3608	0.2259	0.0637
<i>Taylor Green Vortex</i>	0.3715	0.3331	0.4175	0.2525	0.1750	0.1704
	0.1594	0.3057	0.3137	0.1494	0.2362	0.1339

Table 5. LPIPS scores for each dataset. Metrics are reported for both  $32 \times 32 \rightarrow 256 \times 256$  (grey) and  $64 \times 64 \rightarrow 256 \times 256$  tasks.

is governed by three main parameters:  $\beta$  (the maximum importance weight),  $\alpha$  (the minimum importance weight), and  $\theta$  (the importance threshold). We adjust these parameters sequentially. The results are summarized in Figure 15.

### E.6. Comparison of Residual Correction and Post Processing

We compared the performance of residual correction and post-processing technique in Table 6. The post-processing applies a single residual correction to the reconstructed high-fidelity samples in the end. The results indicate that while post-processing achieves very low PDE residuals, it significantly increases the L2 loss. In contrast, our Residual Correction method strikes a better balance between L2 loss and PDE residual.

	L2	PDE Residual
Residual Correction $32 \times 32 \rightarrow 256 \times 256$	2.7897	40.12
Residual Correction $64 \times 64 \rightarrow 256 \times 256$	1.6609	39.97
Post Processing $32 \times 32 \rightarrow 256 \times 256$	3.0019	5.42
Post Processing $64 \times 64 \rightarrow 256 \times 256$	1.7737	7.16

Table 6. Comparison between our proposed Residual Correction and Post Processing methods. Experiments are conducted on the *Kolmogorov Flow*.

### E.7. Generalization

We show the generalization ability of our model across various settings. The original *Kolmogorov Flow* dataset is generated using timestep  $dt = 1/32$ , spatial domain size  $2\pi \times 2\pi$ , and Reynolds number  $Re = 1000$ .

Table 7. Generalization results on *Kolmogorov Flow* dataset with  $64 \times 64 \rightarrow 256 \times 256$  setting.

Variation	Model	L2	Res.
<b>Time Discretization Variations</b>			
$dt = 1/40$	Trained on Original Data	1.6782	31.49
	Trained on $dt = 1/40$ Data	1.6723	30.91
$dt = 1/50$	Trained on Original Data	1.6484	33.49
	Trained on $dt = 1/50$ Data	1.6489	26.66
<b>Spatial Domain Size Variations</b>			
$1\pi \times 1\pi$	Trained on Original Data	1.0255	263.23
	Trained on $1\pi \times 1\pi$ Data	0.9443	207.03
$1.5\pi \times 1.5\pi$	Trained on Original Data	1.3212	84.24
	Trained on $1.5\pi \times 1.5\pi$ Data	1.2918	94.87
<b>Reynolds Number Variations</b>			
$Re = 500$	Trained on Original Data	1.3112	21.57
	Trained on $Re = 500$ Data	1.2998	22.96
$Re = 2000$	Trained on Original Data	1.9647	24.07
	Trained on $Re = 2000$ Data	1.9694	24.22

### E.8. Runtime Comparison

Table 10 presents the time required for the numerical solver to generate a single frame of low- and high-fidelity samples for each dataset. The results indicate that generating even  $64 \times 64$  low-fidelity data is significantly faster than producing high-fidelity data, emphasizing the value of using ML approach for accelerating high-fidelity simulations.

Dataset	$256 \times 256$	$64 \times 64$	$32 \times 32$
<i>Kolmogorov Flow</i>	138.49	0.44	0.04
<i>McWilliams Flow</i>	98.99	1.23	0.12
<i>Decaying Turbulence</i>	93.82	1.01	0.06
<i>Taylor Green Vortex</i>	139.35	1.49	0.22

Table 8. Run time of numerical solver to generate one frame for each dataset across different grid resolutions with a batch size of 10. All times are measured in seconds.

Table 9 shows the time comparison across ML models for reconstructing high-fidelity data from low-fidelity inputs.

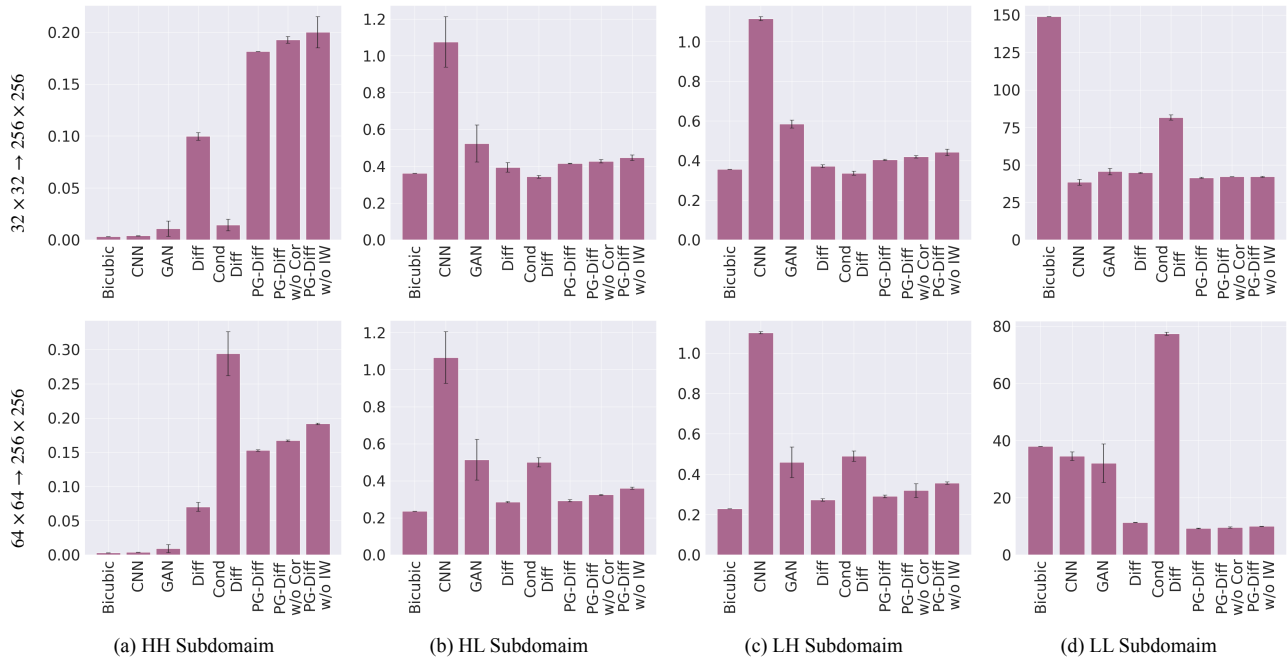


Figure 8. Wavelet subdomain L2 for the *Taylor Green Vortex* dataset.

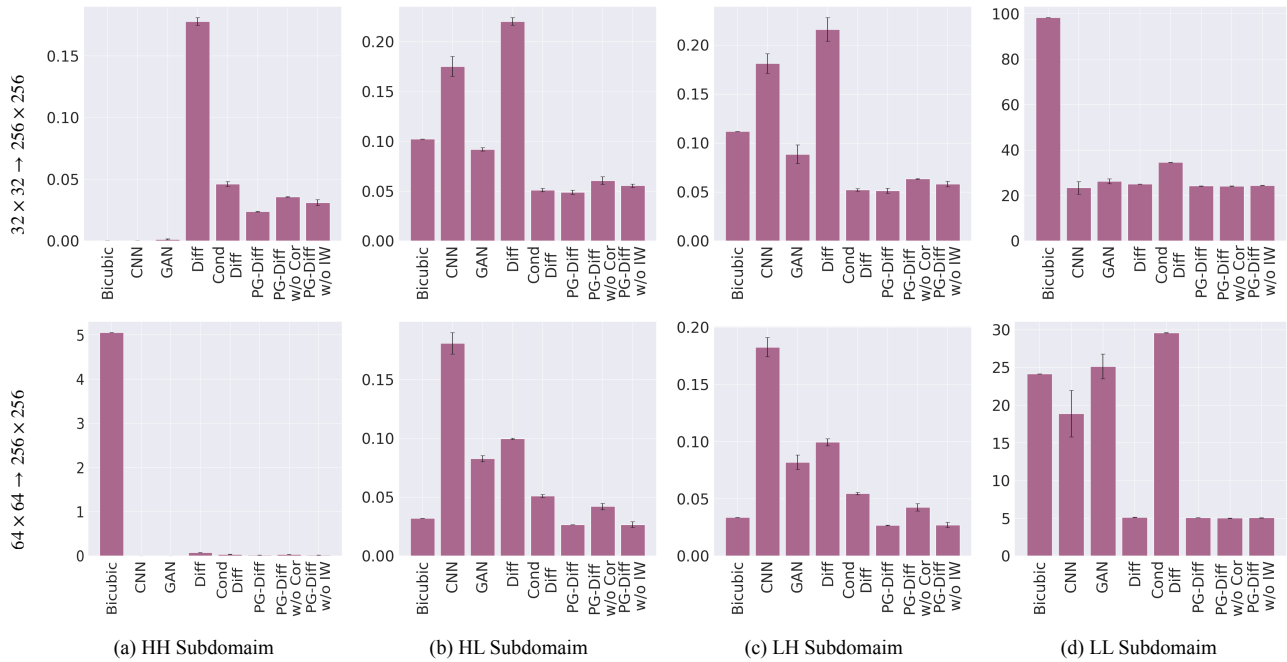


Figure 9. Wavelet subdomain L2 for the *Decaying Turbulence* dataset.

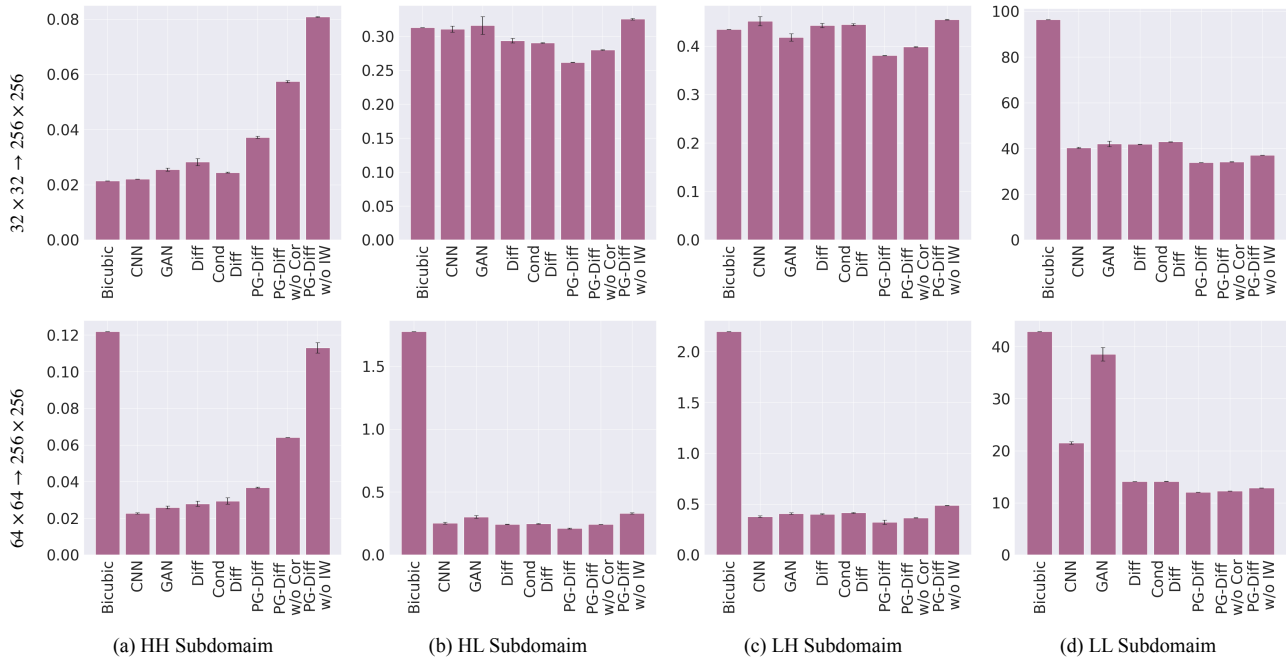


Figure 10. Wavelet subdomain L2 norm for the *Kolmogorov Flow* dataset.

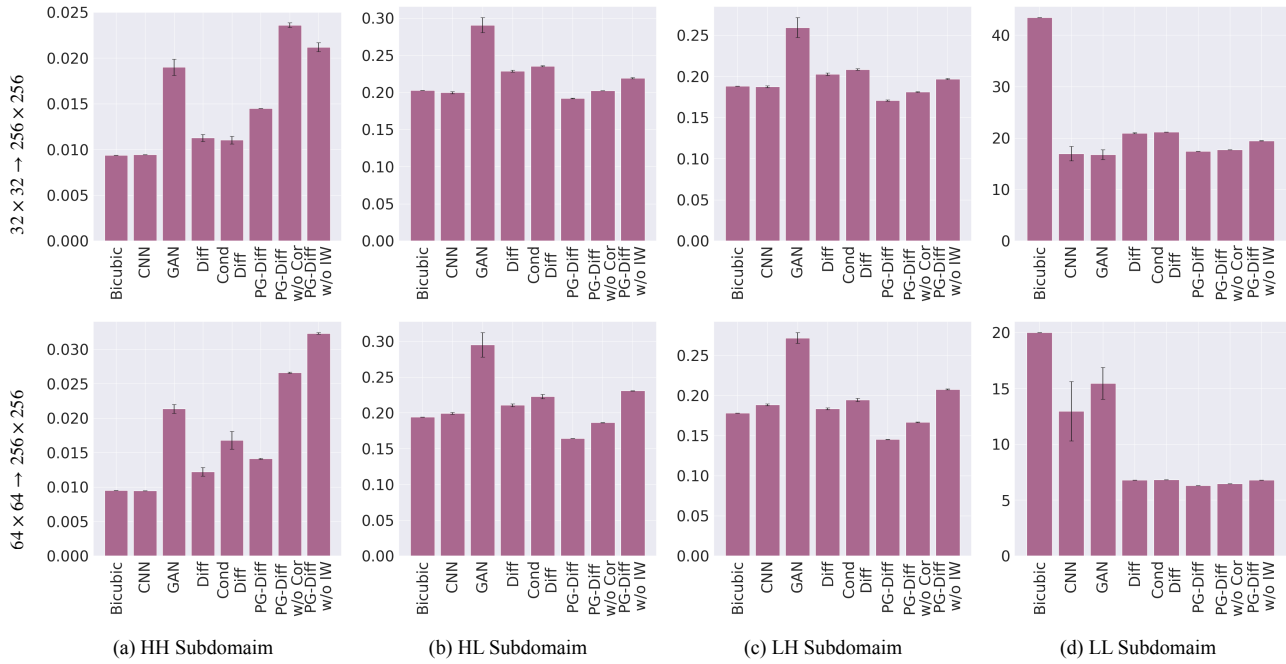


Figure 11. Wavelet subdomain L2 for the *McWilliams Flow* dataset.

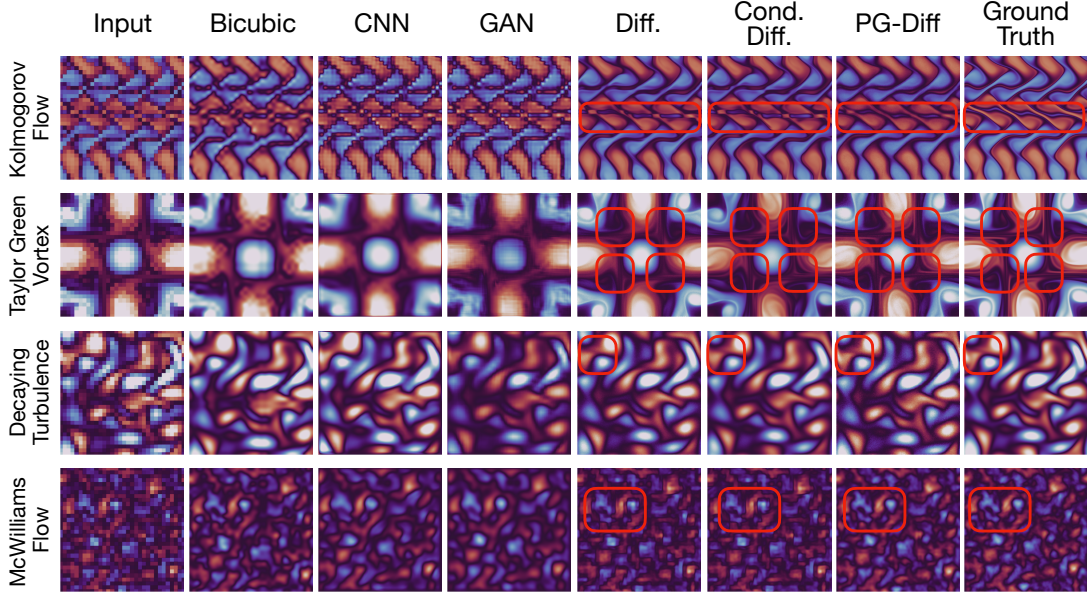


Figure 12. Visualization of reconstructed high-fidelity data across datasets. We highlight fine-grained details where PG-Diff achieves better performance than baseline diffusion models.

Method	$32 \times 32 \rightarrow 256 \times 256$	$64 \times 64 \rightarrow 256 \times 256$
Bicubic	1.43e-5	1.4e-5
CNN	0.005	0.005
GAN	0.008	0.008
Diff	6.10	3.06
Cond Diff	6.20	3.38
PG-Diff	6.37	3.27
<hr/>		
PG-Diff w/o Cor	6.10	3.06
PG-Diff w/o IW	6.37	3.27

Table 9. Runtime comparison of various methods across different resolution levels using a batch size of 10, with all times measured in seconds. These results are based on the *McWilliams Flow* dataset.

Dataset	Same error with $64 \times 64$	Same error with $32 \times 32$
<i>Kolmogorov Flow</i>	35.36	15.15
<i>McWilliams Flow</i>	39.08	17.81
<i>Decaying Turbulence</i>	21.51	17.41
<i>Taylor Green Vortex</i>	33.23	15.49

Table 10. Run time of numerical solver to generate one frame for each dataset with approximately same error compared to PG-Diff with a batch size of 10. All times are measured in seconds.

### E.9. PSNR and SSIM Results

Kolmogorov Flow				
Model	4x Upsampling		8x Upsampling	
	PSNR	SSIM	PSNR	SSIM
Bicubic	21.1257	0.4769	18.3063	0.2479
CNN	24.8310	0.5190	22.9806	0.3712
GAN	20.6210	0.4160	20.2323	0.3695
Diffusion	25.4049	0.6487	21.5818	0.4072
Cond Diff	25.2389	0.6456	20.2067	0.3425
PG-Diff	<b>26.1733</b>	<b>0.6781</b>	<b>24.0754</b>	<b>0.4409</b>

McWilliams Flow				
Model	4x Upsampling		8x Upsampling	
	PSNR	SSIM	PSNR	SSIM
Bicubic	25.1992	0.4834	21.9313	0.2519
CNN	28.6248	0.5897	27.4487	<b>0.5164</b>
GAN	28.6720	0.4621	27.7062	0.4477
Diffusion	29.71018	0.6686	25.2200	0.3884
Cond Diff	29.6757	0.6665	25.1475	0.3823
PG-Diff	<b>30.0540</b>	<b>0.6722</b>	<b>28.1972</b>	0.4643

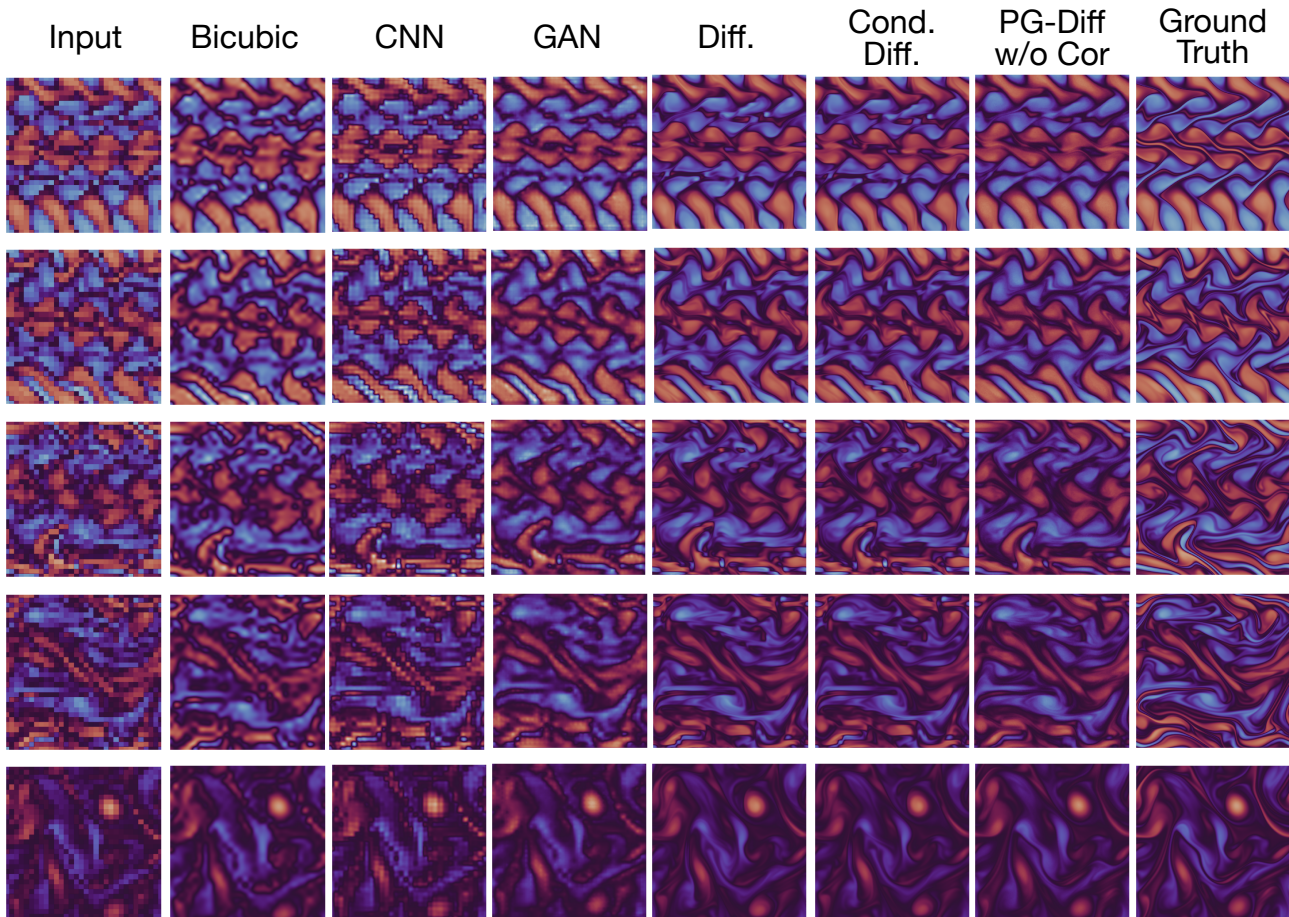


Figure 13. Visualization comparison of reconstruction on the *Kolmogorov Flow* from PG-Diffw/o Cor. The first column displays the low-fidelity input data upscaled to a resolution of  $256 \times 256$ , while the last column shows the high-fidelity ground truth.

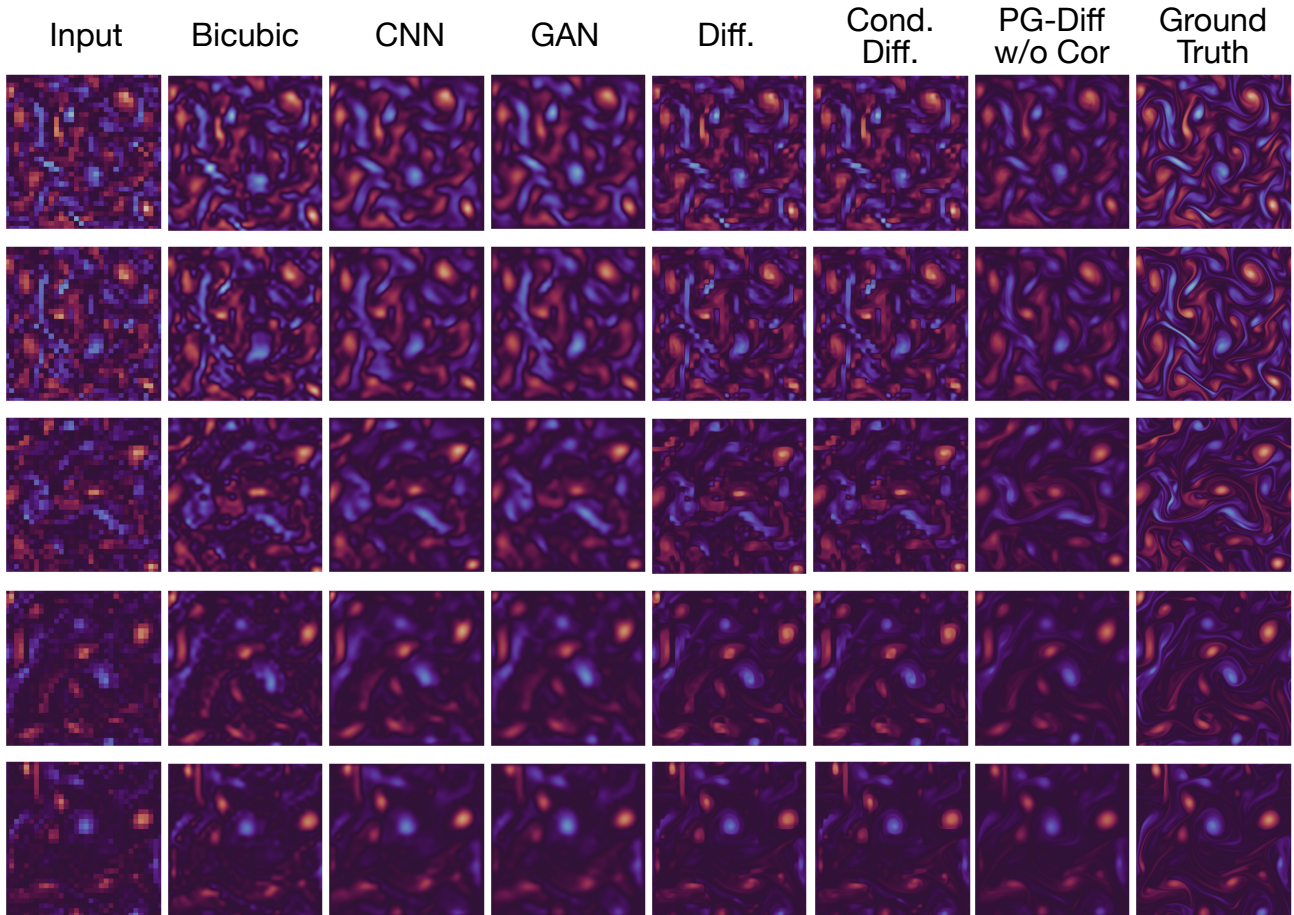


Figure 14. Visualization comparison of reconstruction on the *McWilliams Flow* from PG-Diffw/o Cor. The first column displays the low-fidelity input data upscaled to a resolution of  $256 \times 256$ , while the last column shows the high-fidelity ground truth.

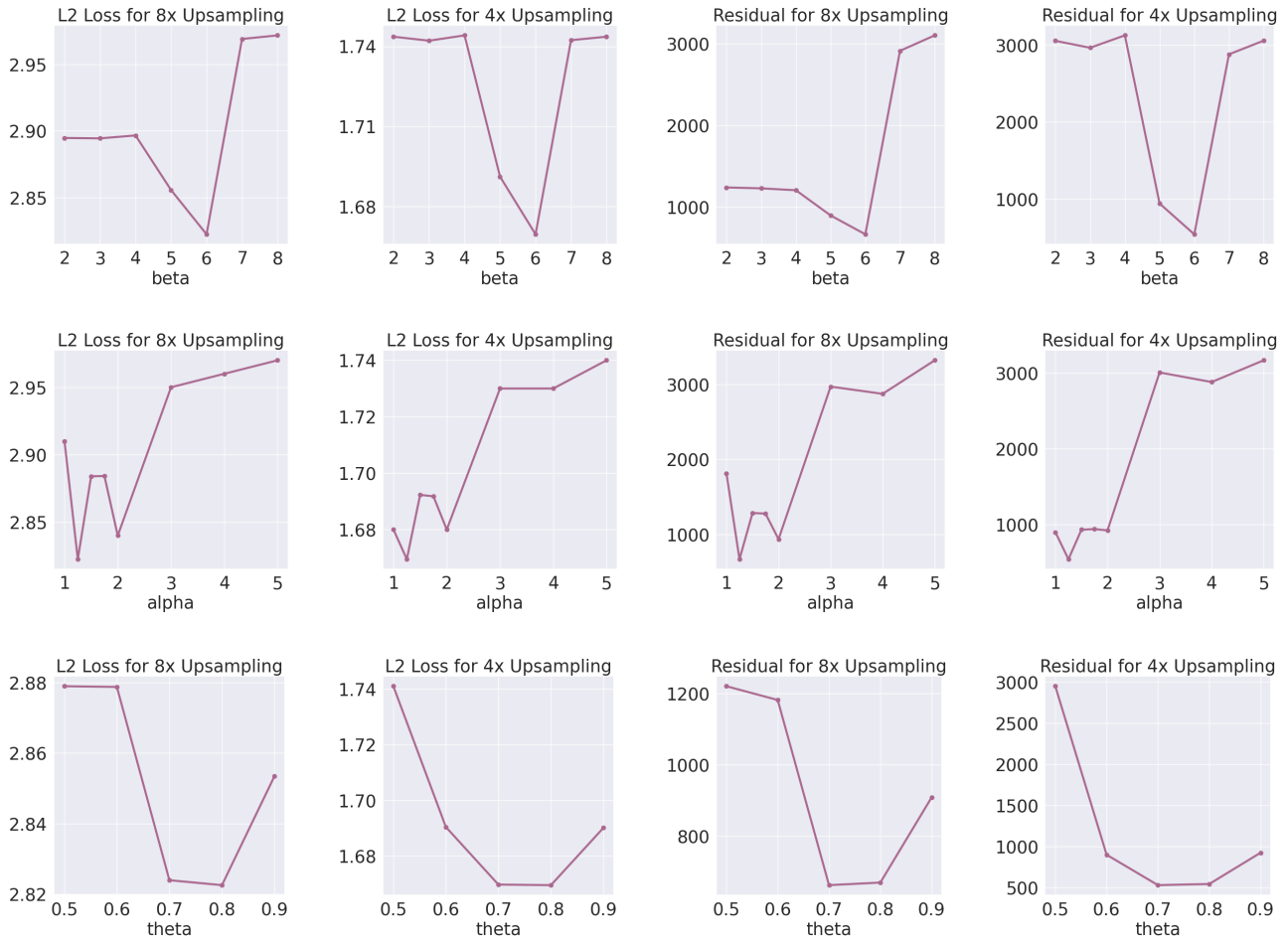


Figure 15. Sensitivity analysis of key parameters for the *Importance Weight*. Experiments are conducted on the *Kolmogorov Flow*. The top row presents the results for the maximum importance weight,  $\beta$ . The middle row displays the results for the minimum importance weight,  $\alpha$ , and the bottom row shows the results for the importance threshold,  $\theta$ . These three hyperparameters were tuned in sequence, and the optimal combination ( $\beta = 6$ ,  $\alpha = 1.25$ , and  $\theta = 0.8$ ) is selected.

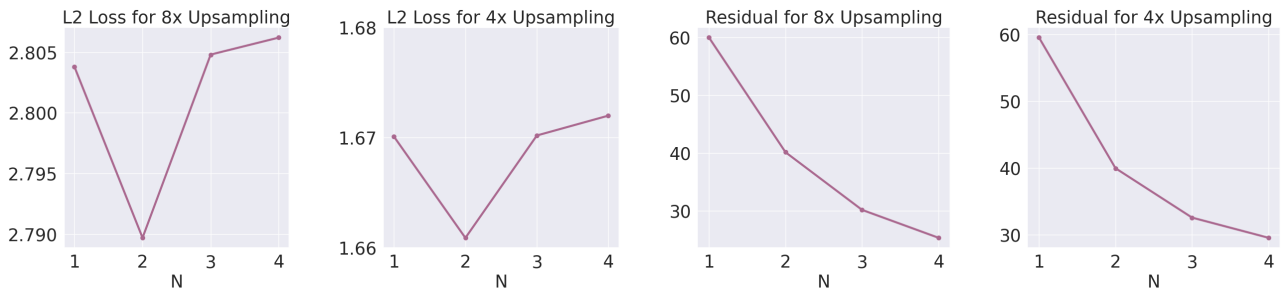


Figure 16. Varying number of  $N$  using the *Start N, End N* correction schedule on the *Kolmogorov Flow* dataset. Showing both L2 and Residual across upsampling settings.

Taylor Green Vortex				
Model	4x Upsampling		8x Upsampling	
	PSNR	SSIM	PSNR	SSIM
Bicubic	25.4811	0.7211	19.4033	0.5041
CNN	26.6066	0.7657	26.3448	0.7422
GAN	28.1370	0.7597	25.0551	<b>0.7633</b>
Diffusion	30.7706	0.8438	24.8698	0.6678
Cond Diff	23.2154	0.6767	21.3979	0.5959
PG-Diff	<b>31.5277</b>	<b>0.8713</b>	<b>26.7503</b>	0.7562

Decaying Turbulence				
Model	4x Upsampling		8x Upsampling	
	PSNR	SSIM	PSNR	SSIM
Bicubic	41.7820	0.8888	35.1032	0.7098
CNN	41.0336	0.8849	42.1580	0.9200
GAN	39.2718	0.9055	38.9931	0.8863
Diffusion	47.2289	0.9571	40.8901	0.8622
Cond Diff	46.0675	0.9138	40.1089	0.8456
PG-Diff	<b>48.0321</b>	<b>0.9601</b>	<b>43.0276</b>	<b>0.9295</b>

### E.10. Proposition Proof

We assume each frame is multivariate gaussian and compare the KL divergence between high-fidelity and solver generated low-fidelity and KL divergence between high-fidelity and downsampled low-fidelity. The low-fidelity data are upsampled uniformly to  $256 \times 256$  when computing the KL divergence. This also matches the methodology used during inference.

	$D_{KL}(p_Y  p_X)$	$D_{KL}(p_Y  q_X)$
<b>Kolmogorov Flow</b>		
$32 \times 32$	207.61	173.07
$64 \times 64$	43.45	36.69
<b>McWilliams Flow</b>		
$32 \times 32$	56.58	39.75
$64 \times 64$	12.26	10.36
<b>Decaying Turbulence</b>		
$32 \times 32$	39.34	33.37
$64 \times 64$	8.65	7.39
<b>Taylor Green Vortex</b>		
$32 \times 32$	9225.79	7741.20
$64 \times 64$	1871.14	1574.79